AGU PUBLICATIONS

Journal of Advances in Modeling Earth Systems

RESEARCH ARTICLE

10.1002/2015MS000618

Key Points:
- A first high-resolution simulation of global water resources and use
- Coupled surface water and groundwater simulation at 10 km by 10 km spatial resolution
- Global hydrological simulations at higher spatial resolutions are feasible for multidecadal periods

Correspondence to:
Y. Wada,
y.wada@uu.nl;
yoshihide.wada@nasa.gov

Citation:
Wada, Y., I. E. M. de Graaf, and L. P. H. van Beek (2016), High-resolution modeling of human and climate impacts on global water resources, *J. Adv. Model. Earth Syst.*, *8*, doi:10.1002/2015MS000618.

Received 24 DEC 2015
Accepted 19 APR 2016
Accepted article online 25 APR 2016

© 2016. The Authors.
This is an open access article under the terms of the Creative Commons Attribution-NonCommercial-NoDerivs License, which permits use and distribution in any medium, provided the original work is properly cited, the use is non-commercial and no modifications or adaptations are made.

High-resolution modeling of human and climate impacts on global water resources

Yoshihide Wada[1,2,3,4], Inge E. M. de Graaf[3,5], and Ludovicus P. H. van Beek[3]

[1]NASA Goddard Institute for Space Studies, New York City, New York, USA, [2]Center for Climate Systems Research, Columbia University, New York City, New York, USA, [3]Department of Physical Geography, Utrecht University, 3584 CS Utrecht, Netherlands, [4]International Institute for Applied Systems Analysis, Laxenburg, Austria, [5]Department of Geology and Geological Engineering, Colorado School of Mines, Golden, Colorado, USA

Abstract A number of global hydrological models [GHMs) have been developed in recent decades in order to understand the impacts of climate variability and human activities on water resources availability. The spatial resolution of GHMs is mostly constrained at a 0.5° by 0.5° grid [∼50km by ∼50km at the equator). However, for many of the water-related problems facing society, the current spatial scale of GHMs is insufficient to provide locally relevant information. Here using the PCR-GLOBWB model we present for the first time an analysis of human and climate impacts on global water resources at a 0.1° by 0.1° grid [∼10km by ∼10km at the equator) in order to depict more precisely regional variability in water availability and use. Most of the model input data (topography, vegetation, soil properties, routing, human water use) have been parameterized at a 0.1° global grid and feature a distinctively higher resolution. Distinct from many other GHMs, PCR-GLOBWB includes groundwater representation and simulates groundwater heads and lateral groundwater flows based on MODFLOW with existing geohydrological information. This study shows that global hydrological simulations at higher spatial resolutions are feasible for multi-decadal to century periods.

1. Introduction

Over the last 100 years, the global population has more than quadrupled and currently exceeds 7 billion. To support the rapidly growing population, and their food demands, economic activities and standard of living, humans have drastically transformed land use and vegetation patterns of the world. Global crop land area has doubled to ∼15 million km^2, while global irrigated area has increased six-fold from ∼0.5 million km^2 to ∼3.0 million km^2 over the last 100 years [*Freydank and Siebert*, 2008]. Increasing population numbers, expanding areas of irrigated agriculture, and associated economic development have driven an ever-increasing demand for water worldwide [*Falkenmark et al.*, 1997; *Oki and Kanae*, 2006; *Hanasaki et al.*, 2008a, 2008b; *Kummu et al.*, 2010; *Vörösmarty et al.*, 2010; *Wisser et al.*, 2010; *Wada et al.*, 2011a, 2011b; *Pokhrel et al.*, 2012; *Elliott et al.*, 2014; *Haddeland et al.*, 2014]. Global water use (i.e., withdrawal) has increased by nearly 8 times from ∼500 km^3 yr^{-1} to ∼4000 km^3 yr^{-1} over the last 100 years, with an acute increase at a rate of ∼15% per decade between 1960 and 2010. Agriculture, mostly irrigation, is the principal user of water and accounts for ∼70% of the global total, with the remaining part attributable to the industrial and domestic sectors [*Döll and Siebert*, 2002; *Bondeau et al.*, 2007; *Gerten et al.*, 2007; *Rost et al.*, 2008; *Wisser et al.*, 2008; *Liu and Yang*, 2010; *Siebert and Döll*, 2010; *Siebert et al.*, 2010; *de Graaf et al.*, 2014].

To satisfy their needs, humans extract vast amounts of water from surface water and groundwater resources. To boost surface water availability, tens of thousands of reservoirs have been constructed in many tributaries of the major rivers and their total storage capacities exceed ∼8000 km^3 worldwide [*Lehner et al.*, 2011]. A number of reservoirs also serve as the source of hydropower generation to supply the energy needs for industries and to support the increased standard of living over various regions. Nevertheless, soaring human water use has caused conditions of water scarcity in regions including India, Pakistan, Western and Central United States, Northeast China, Iran, the Middle East and North Africa, and Southern Europe [*Gleick*, 2003, 2010; *Vörösmarty et al.*, 2010; *Oki and Kanae*, 2006; *Hanasaki et al.*, 2008a, 2008b; *Kummu et al.*, 2010; *Hoekstra et al.*, 2012; *Schewe et al.*, 2014; *Gain and Wada*, 2014]. In such regions, the water demand exceeding the available surface freshwater resources is often supplemented by groundwater resources.

Excessive groundwater pumping, however, often leads to overexploitation, causing groundwater depletion [*Konikow and Kendy*, 2005; *Rodell et al*., 2009; *Tiwari et al*., 2009; *Famiglietti et al*., 2011; *Konikow*, 2011; *Döll et al*., 2012; *Scanlon et al*., 2007, 2012a, 2012b; *Wada et al*., 2012a, 2012b; *Taylor et al*., 2013] that may have devastating effects on environmental streamflow, groundwater-fed wetlands and related ecosystems [*Gleeson et al*., 2012; *Gleeson and Wada*, 2013; *Wada and Heinrich*, 2013] As a result, terrestrial water fluxes have been affected by humans at an unprecedented scale and the fingerprints that humans have left on Earth's water resources are turning up in a diverse range of records and can be seen in surface freshwater (water in rivers, lakes, reservoirs and wetlands) and groundwater resources alike [*Van Dijk et al*., 2014].

Multi-decadal climate variability also has substantial impacts on Earth's water resources. In several parts of the world (e.g., Asia, Africa), drought is closely associated with the presence of the El Niño-Southern Oscillation (ENSO) that has driven a number of severe drought events [*Trenberth et al*., 1988; *Seager*, 2007; *Sheffield and Wood*, 2007; *Sheffield et al*., 2012; *Dankers et al*., 2014; *Prudhomme et al*., 2014]. There is a growing concern that the natural patterns of climate have been altered due to increasing anthropogenic forcing (e.g., greenhouse gas emission and intense irrigation). Changing climate is in turn expected to alter the water cycle (e.g., the rate of evapotranspiration and the amount of precipitation), and subsequently impact regional water resources [*Arnell*, 1999, 2004; *Alcamo et al*., 2007; *Feyen and Dankers*, 2009; *Jung et al*., 2010; *Dai*, 2011, 2013].

To simulate terrestrial water fluxes and storage (water in rivers, lakes, wetlands and reservoirs), consistently across the globe, a number of land surface models (LSMs) and global hydrological models (GHMs) have been developed in recent decades. LSMs generally have a simplified treatment of the surface hydrology and do not include human-induced change, primarily focusing on the interactions of land-atmosphere processes for climatic simulations in general circulation models (GCMs). Notable examples of LSMs include VIC [*Wood et al*., 1992] and Noah [*Ek et al*., 2003]. GHMs have a detailed representation of terrestrial hydrological processes at long temporal and fine spatial resolutions, and in general include human-induced change (e.g., human water use and reservoir regulation). Examples of GHMs are H08 [*Hanasaki et al*., 2008a, 2008b], MATSIRO [*Pokhrel et al*., 2012], PCR-GLOBWB [*Van Beek et al*., 2011; *Wada et al*., 2014], WADMOD-M [*Widén-Nilsson et al*., 2007], WaterGAP [*Alcamo et al*., 2007], WGHM [*Döll et al*., 2003] and WBMplus [*Wisser et al*., 2010]). Distinct from LSMs and GHMs, Dynamic Vegetation Models (DVMs) include a simplified treatment of the surface hydrology but a special treatment on biosphere that enables quantitative assessment of transient changes in vegetation and land surface hydrology in response to variations in climate and anthropogenic CO_2 increase. LPJmL [*Gerten et al*., 2007] and DBH [*Tang et al*., 2007] fall into this category.

GHMs typically simulate the dynamics of soil moisture storage due to changes in precipitation and evapotranspiration, the generation of runoff and the discharge through the river network at a 0.5° by 0.5° global grid (~50km by ~50km at the equator) where climate, physiographic, and socio-economic data are most available. The majority of GHMs are based on the water balance concept and track the transfer of water through a number of stores with time steps ranging from a month to less than 1 day. Conceptual models are chosen as they are deemed to be more robust than empirical models and more parsimonious in their data requirements than fully physically based models, whilst they maintain the ability to translate reliably the effects of global change on the hydrology in a consistent manner. With their development, the process descriptions in GHMs have become more physically based and their spatial and temporal resolution have increased. Nevertheless, for many of the water-related problems facing society, the current spatial scale of the models is insufficient to provide locally relevant information as well as to better solve the mechanisms [*Wood et al*., 2011; *Bierkens et al*., 2015]. For example, modeling and prediction of effects of human activity on the water cycle require accurate spatial representation of water extractions, irrigation, and reservoir management. Modeling the hydrodynamic effects of drought and flood needs a higher resolution modeling framework. Recent improvement in computational capabilities has outrun the capabilities, and theoretical underpinnings, of the current generation of models. Higher spatial resolutions are demonstrably feasible for multi-decadal to century simulations.

Here we present for the first time an analysis of human and climate impacts on global water resources at a 0.1° by 0.1° global grid (~10km by ~10km at the equator). This is a finer spatial resolution than those of any previous global scale assessments, and enables us to depict more precisely regional variability in water availability and use. Over the period 1960–2010 we use the global hydrological and water resources model PCR-GLOBWB (version 2.0) [*Van Beek et al*., 2011; *Wada et al*., 2014] that runs at a daily temporal resolution

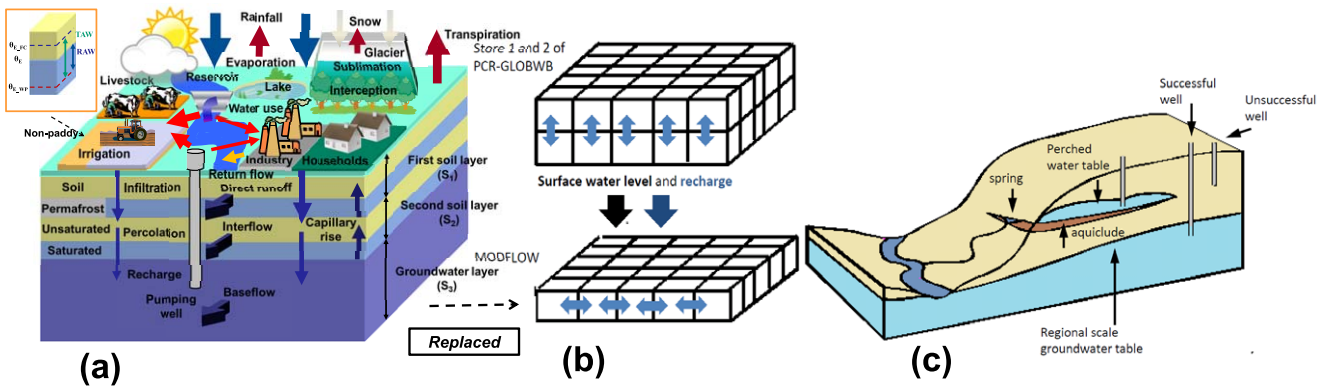

Figure 1. Schematic diagram of the integrated modeling framework: (a) general PCR-GLOBWB model setup, (b) model structure used to couple the land-surface model PCR-GLOBWB with the groundwater model MODFLOW: first average annual net recharge and average annual channel discharge is calculated with PCR-GLOBWB. The latter is translated into surface water levels. Both recharge and surface water levels are used to force MODFLOW, and (c) cross section illustrating the difference between the simulated regional scale groundwater table and often sampled perched water table.

and has enhanced the spatial resolution of the model globally from 0.5° to 0.1°. Most model input data have been parameterized at a 0.1° global grid and feature a distinctively higher resolution. With the enhanced spatial resolution of input parameters including topography, vegetation, soil properties and lithology, the process representations of hydrological fluxes (e.g., runoff generation, infiltration, percolation) have been substantially improved. Channel characteristics for river routing have also been derived from a high-resolution drainage direction map. Moreover, human activities such as human water use from agriculture (i.e., livestock and irrigation), industry, households, and reservoir regulation have been parameterized at a 0.1° grid, using the latest available spatially explicit data of livestock densities, irrigated areas, population numbers and the location of reservoirs.

Distinct from many other GHMs, our model considers groundwater representation that is crucial to assess groundwater resources. To understand groundwater table fluctuations caused by changes in climate and human water use, lateral groundwater flows and groundwater-surface water interactions such as river infiltration should be included in current hydrological modeling efforts, especially at finer resolutions [*Wood et al.*, 2011]. Although groundwater flows are often slow, they regularly cross topographic and administrative boundaries at applicable rates. These inter-basin groundwater flows increase water availability in water receiving catchments or aquifers and help to maintain baseflows and shallow groundwater tables during droughts [*de Graaf et al.*, 2015]. In this study we simulate groundwater heads, lateral groundwater flows and groundwater-surface water interactions and pioneer with abstractions. The effects of groundwater abstractions on groundwater heads, base flows, and aquifer's water budgets are studied. A global scale lateral groundwater model developed by *de Graaf et al.* [2015] is coupled to the PCR-GLOBWB model by replacing the original groundwater store (S3; see Figure 1). The model is based on MODFLOW [*Harbaugh et al.*, 2000] and describes an upper unconfined aquifer. The aquifer parameterization included geohydrological information for the first time (aquifer thickness and transmissivity), however data are sparse and incomplete. To overcome this lack of data, only global data sets are used, such that the parameterization method can be expanded to data-poor environments. In this study the model is run at steady state (averaged over 1960–2010) for pristine and human conditions.

Alternative water resources such as desalinated water use has also been incorporated in our model. The impact of human-induced change has been dynamically simulated at a daily time step, considering the feedback among water availability, water extractions, return flow to the river network and soil system, and evapotranspiration (e.g., from irrigation) [*Wada et al.*, 2014].

Section 2 of this paper presents a brief description of the model and associated model parameterization at 0.1° global grid, and the simulation protocol. Section 3 presents the simulation results. Section 4 evaluates the model performance by comparing the simulation results to available statistics and satellite information. Section 5 discusses the advantages and the limitations of the higher-resolution modeling framework and the associated uncertainties, and provides conclusions from this study.

2. Models, Data, and Methods

2.1. High-Resolution PCR-GLOBWB Model––Water Balance

Figure 1 shows a schematic diagram of the global hydrological and water resources model PCR-GLOBWB (version 2.0) that integrates human activities including water use and reservoir regulation into hydrology at a daily temporal resolution. For the detailed description of the basic hydrologic model structure and associated calculation, and water use calculation, we refer to *Van Beek et al*. [2011] and *Wada et al*. [2014]. Below, we briefly present the main features of the model, separately for hydrologic and water use calculation, and the model parameterization at a 0.1° by 0.1° globally over the land excluding the Antarctic (∼10km by ∼10km at the equator).

PCR-GLOBWB simulates for each grid cell and for each time step (daily) the water storage in two vertically stacked soil layers and an underlying groundwater layer, as well as the water exchange between the layers (infiltration, percolation, and capillary rise) and between the top layer and the atmosphere (rainfall, evapotranspiration, and snow melt). The model also calculates canopy interception and snow storage. Sub-grid variability is taken into account by considering separately tall and short vegetation, paddy rice, nonpaddy crops, rainfed crop, open water (lakes, reservoirs, floodplains and wetlands), different soil types based on the FAO Digital Soil Map of the World [*Food and Agriculture Organization of the United Nations (FAO)*, 2003], and the area fraction of saturated soil calculated by Improved ARNO scheme [*Todini*, 1996; *Hagemann and Gates*, 2003] as well as the frequency distribution of groundwater depth based on the surface elevations of the HYDRO1k Elevation Derivative Database (HYDRO1k; U.S. Geological Survey Center for Earth Resources Observation and Science; https://lta.cr.usgs.gov/HYDRO1K/). Each of the land cover types has different hydrological fluxes (e.g., runoff, evaporation, transpiration). Particular rock and geological formations like fissures and karsts are not included in the model. Precipitation is subject to interception, evapotranspiration, and infiltration to the soil layers. Infiltration rates are determined by soil storage capacity and, the rates of saturated or unsaturated soil hydraulic conductivity. Vapor or thermal conductivity in the soil is not represented in the modeling framework. The groundwater layer represents the deeper part of the soil that is exempt from any direct influence of vegetation and constitutes a groundwater reservoir fed by active recharge. The groundwater store is explicitly parameterized based on lithology and topography. Natural groundwater recharge fed by net precipitation, and additional recharge fluxes from irrigation, i.e., return flow, fed by irrigation water supply and from industrial and domestic sectors occurs as the net flux from the lowest soil layer to the groundwater layer, i.e., deep percolation minus capillary rise. Groundwater recharge interacts with groundwater storage by capillary rise and baseflow. The model calculates capillary rise if the top of the groundwater level is within 5 m of the topographical surface (calculated as the height of the groundwater storage over the storage coefficient on top of the streambed elevation and the sub-grid distribution of elevation). Groundwater storage is fed by groundwater recharge and drained by a reservoir coefficient that includes information on lithology and topography (e.g., hydraulic conductivity of the subsoil). The ensuing capillary rise is calculated as the upward moisture flux that can be sustained when an upward gradient exists and the moisture content of the soil is below field capacity. Also, it cannot exceed the available storage in the underlying groundwater reservoir. In this study, an original linear reservoir model [*Kraijenhoff van de Leur*, 1958] has been replaced by a lateral groundwater flow model based on MODFLOW [*Harbaugh et al*., 2000] that was developed by *de Graaf et al*. [2015] and *Sutanudjaja et al.* [2014].

The parameterization of the vegetation relies on the Global Land Cover Characteristics Data Base Version 2.0 (GLCC 2.0; http://edc2.usgs.gov/glcc/globe_int.php/) available at a ∼0.01° spatial resolution (∼1km by ∼1km at the equator) and the land surface parameter data set (LSP2) [*Hagemann*, 2002]. Associated soil properties are derived from the vector-based FAO Digital Soil Map of the World (DSMW) [*FAO*, 2003] that is gridded at a ∼0.01° spatial resolution, and the WISE data set of global soil properties (ISRIC-WISE) [*Batjes*, 2005]. These finer spatial resolution data sets have been used to derive the sub-grid variability within each grid cell. The maximum rooting depth used to obtain root content, the shape parameter b of the improved Arno scheme, and the fractional vegetation cover and corresponding maximum interception storage capacity have been derived from the GLCC 2.0 and the LSP2. From the DSMF and the ISRIC-WISE, soil properties including saturated hydraulic conductivity, saturated and residual (volumetric) water contents, porosity, air entry value, and coefficient β of the soil water retention curve have been derived for each soil class for two different depths, i.e., from 0 to 30 cm (first soil layer) and from 30 to 150 cm (second soil layer). These values have been first aggregated at the pedon level, where up to 8 soil classes and their fractional

cover are specified per pedon at the spatial resolution of 0.1°. The two soil layers represent the first and second store of the model except in those areas where soil formation is limited by bedrock or impeding layers, in which the two layers were reduced proportionally. For the third store of infinite capacity, the recession constant has been estimated on the basis of the lithology and distance to the drainage network derived from the HYDRO1k, which is also used to determine the slope length (L_s) and slope tan(α_s).

2.2. High-Resolution PCR-GLOBWB Model––Water Demand and Use

Water demands are calculated for agricultural (livestock and irrigation), industrial and domestic sectors over the period 1960–2010. The gridded global livestock density for cattle, buffalo, sheep, goats, pigs and poultry available at a 0.05° spatial resolution (~5km by ~5km at the equator) [*Food and Agriculture Organization of the United Nations (FAO)*, 2007] for the year 2000 have been aggregated to 0.1°. We then combine these with their corresponding daily drinking water requirements [*Steinfeld et al*., 2006] that are a function of daily air temperature [*Wada et al*., 2011a, 2011b]. To consider the historical growth of livestock densities, the numbers of each livestock type per country (FAOSTAT; http://faostat.fao.org/) have been downscaled to a grid scale using the distribution of each gridded livestock density of the year 2000. A daily irrigation scheme has been implemented that separately parameterizes paddy and non-paddy crops and that dynamically links with hydrological fluxes considering the feedback between the application of irrigation water and the corresponding changes in surface and soil water balance, and evapotranspiration [*Wada et al*., 2014]. The losses (i.e., return flow) during water transport and irrigation application are included in the simulation based on daily evaporative and percolation losses per unit crop area based on the surface and soil water balance. Crop-specific calendars, growing season lengths and irrigated areas are obtained from the MIRCA2000 data set [*Portmann et al*., 2010] that is available at a ~0.1° spatial resolution. The corresponding crop coefficient per crop development stage and maximum crop rooting depth were additionally obtained from the Global Crop Water Model [*Siebert and Döll*, 2010]. The MIRCA2000 data set accounts for growing seasons of 26 different crop classes and regional cropping practices under different climatic conditions, but we have aggregated these to paddy and non-paddy crop classes since distinct flooding irrigation is applied over most of paddy fields. The crop-specific parameters have been aggregated by weighing the area of each crop class. Historical growth of irrigated areas is estimated using country-specific statistics of irrigated areas for ~230 countries (FAOSTAT) and by downscaling these to 0.1° using the spatial distribution of the gridded irrigated areas from the MIRCA2000 data set [*Portmann et al*., 2010]. This method is unable to reproduce changes in the distribution within countries, but it only reflects the large-scale dynamics of the intensifying irrigated areas over the past decades.

For the industrial sector, we calculate country-specific water use intensities on the basis of economic development and technological improvement [*Wada et al*., 2011a]. Economic development is approximated using four socio-economic variables: Gross Domestic Product (GDP), electricity production, energy consumption, and household consumption. Technological development is then approximated by energy consumption per unit electricity production, which accounts for industrial restructuring or improved water use efficiency, since an increase in industrial water use slows down after reaching a certain technological advancement. Reference water demand data for the year 2000 have been obtained from *Shiklomanov* [1997], *World Resources Institute* (*WRI)* [1998], and *Vörösmarty et al*. [2005] and combined with the estimated water use intensities over the period 1960–2010. Estimated industrial water demand is eventually gridded to 0.1° using the night-time light intensities that are obtained from the National Oceanic and Atmospheric Administration (NOAA)'s National Geophysical Data Center (http://www.ngdc.noaa.gov/) available at a ~0.01° spatial resolution. Due to limited available data in order to identify the seasonal trends, daily industrial water demands have been kept constant over the year [*Hanasaki et al*., 2008a, 2008b; *Wada et al*., 2011a, 2011b). Domestic water demand is estimated by multiplying the number of persons in a grid cell with the country-specific per capita domestic water extraction (FAO AQUASTAT database; http://www.fao.org/nr/water/aquastat/main/index.stm/). The daily water demand variations are determined using daily air temperature as a proxy [*Wada et al*., 2011a]. The country per capita domestic water extraction in 2000 is multiplied with the estimated water use intensities to account for economic and technological development. Gridded global population maps per decade at a 0.1° spatial resolution [*Klein Goldewijk and van Drecht*, 2006] have been used to downscale the annual country population data (FAOSTAT) to produce gridded population maps for each year over 1960–2010.

2.3. High-Resolution PCR-GLOBWB Model––Routing and Water Allocation

The simulated local direct runoff, interflow, and baseflow are routed along the drainage network based on channel characteristics at a 0.1° spatial resolution derived from the HydroSHEDS data set (http://hydrosheds.cr.usgs.gov/index.php/). The drainage network above 60°N has been supplemented using the Simulated Topological Networks [*Vörösmarty et al.*, 2000] and the topographic data from the HYDRO1k. The routing is based on the characteristic distances, where volumes of water are transported over a distance [*Wada et al.*, 2014]. Reservoirs are located on the drainage network based on the newly available and extensive Global Reservoir and Dams Dataset (GRanD) [*Lehner et al.*, 2011] that contains 6,862 reservoirs with a total storage capacity of 6,197 km^3. The reservoirs have been placed over the river network based on the years of their construction. If more than one reservoir fell into the same grid cell, we have aggregated the storage capacities and modeled a single reservoir. Similar to *Hanasaki et al.* [2006] and *Van Beek et al.* [2011], reservoir release is simulated to satisfy local and downstream water demands that could be reached within ~600km (~a week with an average discharge velocity of 1 m s^{-1}) or a next downstream reservoir if present. In case of no water demand, the reservoir release is simulated as a function of minimum (set to ~10% of storage capacity), maximum (set to ~100% of storage capacity), and actual reservoir storage and mean average inflow. Reservoir spills occur when the reservoir storage exceeds the maximum reservoir storage.

Water demands for livestock, irrigation, industry and households (see section 2.2.) can be met from three water resources; 1) desalination, 2) groundwater, and/or 3) surface water. Desalinated water use is generally limited to coastal areas, but provides a stable amount of water supply over water-scarce regions such as the Middle East and North Africa, where over 70% of the global desalination capacity is installed. We use available country statistics of desalination water withdrawal for the period 1960–2010 from the FAO AQUASTAT database and the WRI EarthTrends [*WRI*, 1998, http://www.wri.org/project/earthtrends/] (global total $\approx$ 15 km^3 yr^{-1}). We limit desalinated water use over a global coastal area of ~40km and downscale the country statistics based on the associated gridded population intensities over the coast. Allocation of surface water and groundwater to satisfy the remaining water demand (after subtracting desalinated water withdrawal) depends on available surface water including local and upstream reservoirs and readily extractable groundwater reserves. Since the absolute amount of available groundwater resources is not known at the global scale, we have used the simulated daily (accumulated) baseflow against the long-term average river discharge as a proxy to infer the readily available amount of renewable groundwater reserves [*Wada et al.*, 2014]. The remaining water demand is then withdrawn from the simulated surface water. However, in case reservoirs are present at local or upstream grid cells over the river network, we first allocate surface water rather than groundwater to meet the water demand, and the remaining water demand is met from available groundwater storage. In case of no outstanding water demand, no groundwater is abstracted. The unmet water demand is then imposed on (nonrenewable) groundwater (e.g., groundwater withdrawal in excess of available groundwater storage). The available water is allocated proportionally to the amount of sectoral water demands. No priority is given to a specific sector, but a competition of water use among the sectors likely occurs over many water scarce regions, particularly for surface water resources.

After water is withdrawn for the irrigation, industrial and domestic sectors, return flow occurs to the river system. No return flow to the soil or river system occurs from the livestock sector. For the irrigation sector, return flow (losses) during water transport and irrigation application are simulated based on daily evaporative and percolation losses based on the surface and soil water balance (see section 2.2.). Irrigation return flow is dominated by percolation losses to groundwater (>90%), while the return flow to direct runoff is small. After the irrigation return flow reaches to the groundwater storage, the water is drained to baseflow by a reservoir coefficient (residence time from days to hundreds' years; see section 2.1.) that causes delayed response in river discharge. For the industrial and domestic sectors, return flow occurs on the same day (no retention due to waste water treatment). For the domestic sector, the return flow occurs only from the areas where urban and rural population have access to water (UNEP; http://www.unep.org/), whereas for the industry sector, the return flow occurs from all areas where water is withdrawn. For both sectors, the amount of return flow is determined by recycling ratios developed per country. The country-specific water recycling is calculated according to the method developed by *Wada et al.* [2011a, 2011b] who interpolate recycling ratios on the basis of GDP and the level of economic development, i.e., high income (80%; 20% of water is actually consumed.), middle income (65%; 35% of water is consumed.), and low income economies (40%; 60% of water is consumed.). A ratio is kept at 80% if a country reached the high income economy, and the ratio of 40% has been assigned to countries with no GDP data. For completeness, we note that consumptive water use is equal to water withdrawal minus return flow.

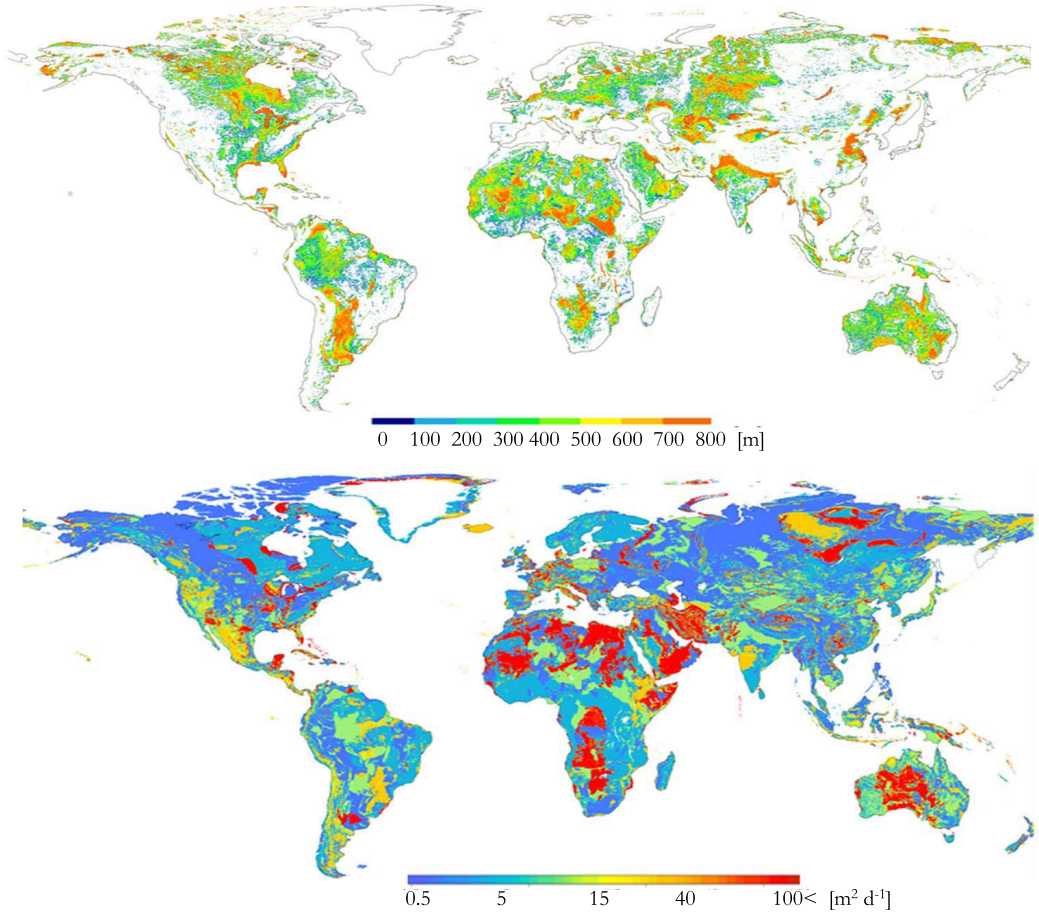

Figure 2. Estimated aquifer thickness and transmissivities [*de Graaf et al*., 2015].

2.4. High-Resolution PCR-GLOBWB Model––Groundwater Flow Representation

A global-scale lateral groundwater flow model [*de Graaf et al*., 2015] is coupled to simulated groundwater heads and lateral flows at the steady state. The linear groundwater store of PCR-GLOBWB (S3 in Figure 1) is replaced by a one-layer MODFLOW model [*Harbaugh et al*., 2000]. Aquifer properties are prescribed, describing an upper unconfined aquifer. The MODFLOW model is forced with recharge and river discharge outputs from PCR-GLOBWB (Figure 1) averaged over 1960–2010. In case of human water use these inputs include return flows to groundwater and surface water (i.e., abstracted water that is not consumed). Groundwater-surface water interactions are incorporated using MODFLOW's river and drain packages, drain levels were calculated from river discharges. Three drain levels are distinguished; (1) larger rivers, with a width greater than 25m, (2) smaller rivers, with a width smaller than 25m, and (3) springs and streams higher up in the valley (for more details, see *de Graaf et al*. [2015]). Gross groundwater abstractions were included in MODFLOW's well package.

The aquifer parameterization is adopted from *de Graaf et al*. [2015] that includes geohydrological information for the first time. However, data are scarce and incomplete for many regions of the world. Therefore, the parameterization is fully based on available global data sets on lithology [*Hartmann and Moosdorf*, 2012] and permeability [*Gleeson et al*., 2011, 2014] and an estimate of aquifer thickness (Figure 2), such that the parameterization methods can be expanded to data-poor regions and stay relative simple. Aquifer thicknesses are estimated using terrain attributes, based on the assumption that productive aquifer coincide with sediment basins below river valleys. The distinction was made between (1) mountain ranges and (2) sediment basins. The thickest aquifer layers can be found for the world's major river basins, like Mississippi and Ganges. Corresponding transmissivities (Figure 2).

2.5. Model Simulation

To assess the impact of human-induced change (i.e., water use and reservoir regulation) on global water resources, we perform two separate simulation runs. The first run evaluates global water resources under natural conditions with climate variability only, thus with no human activities (hereafter, *pristine*), while the second run evaluates global water resources under climate variability and with human activities (hereafter, *humans*). We thus analyze the transient effect of human water use and reservoir regulation by comparing the pristine and the humans' simulation runs over the period 1960–2010.

The model is forced with daily fields of precipitation, reference (potential) evapotranspiration and temperature. For the period 1960–1978, precipitation and temperature were prescribed by the ERA40 reanalysis data [*Uppala et al*., 2005]. Over the same time period, prescribed reference evapotranspiration is calculated based on the Penman-Monteith equation according to the FAO guidelines [*Allen et al*., 1998] with relevant climate fields (e.g., cloud cover, vapor pressure, wind speed) retrieved from the ERA40 reanalysis data. To extend our historical analysis to the year 2010, we force the model by comparable daily climate fields taken from the ERA-Interim reanalysis data [*Dee et al*., 2011]. From the ERA-Interim data set, we obtain daily fields of temperature and GPCP-corrected precipitation (GPCP: Global Precipitation Climatology Project; http://www.gewex.org/gpcp.html/), and calculate reference evapotranspiration by the same method retrieving relevant climate fields. For compatibility with our overall analysis, the ERA40 reanalysis data are bias-corrected on a grid-by-grid basis by scaling the long-term monthly means of the daily climate fields (precipitation, evapotranspiration and temperature) to those of the ERA-Interim re-analysis data for the overlapping reference climate 1979–2001. We then further bias-correct the modified climate data set by scaling the long-term monthly means of the daily climate fields to those from the CRU TS 2.1 data set [*Mitchell and Jones*, 2005], wherever station coverage by the CRU is adequate for the overlapping period. Otherwise the original (modified) climate data are returned by default. For the ERA40 reanalysis data, we bias-correct separately for the 1960s and 1970s to correct the overestimation of precipitation present over the tropics during the 1970s [*Uppala et al*., 2005]. The resulting bias-corrected transient daily climate fields are used to force the model over the period 1960–2010. In order to represent the fine transition over 0.1° grid elevation dependent gradients of temperature, 10 elevation zones have been imposed on each grid cell based on the HYDRO1k, and scaled to the 0.5° grid temperate fields with a lapse rate of 0.65°C per 100m.

To test the model performance, simulated groundwater heads are compared to a compilation of reported data worldwide [*Fan et al*., 2013]. If more than one observation was available within a 0.1° grid cell, the average of that cell has been used, resulting in 65,303 cells with observations. Groundwater heads are evaluated instead of depths as heads measure the potential energy driving flow and are therefore physically more meaningful. The coefficient of determination (R^2) and regression coefficient (α) are calculated for the two runs (pristine and humans).

[24] Baseflow magnitudes and patterns change due to abstraction and return flows compared to the pristine run. A simple method to analyze the change in base flow magnitude is to calculate the ratio between base flow and groundwater recharge; Qbase: R. In this study this is done for aquifers of the world (from WHYMAP; http://www.whymap.org/). For the natural situation if Qbase equals R the ratio is 1, all water going in is going out over the same area. If more water is drained than recharged (Qbase: $R < 1$), water is imported from neighboring areas outside the aquifer. If less water is drained than recharged (Qbase: $R > 1$) water is exported to neighboring areas. When abstractions are included, groundwater is consumed from the groundwater store, groundwater levels drop and baseflow magnitudes decline. Less water is drained and flow path patterns change. Additional return flows reduce this effect, however the effects can still be devastating especially during droughts. The degree of deviation from 1 depends on several factors; larger deviations are found for smaller aquifers, regions with little recharge, and aquifers with thick, more permeable, dipping layers [*Schaller and Fan*, 2008].

3. Results

3.1. High-Resolution Global Water Use Estimates

3.1.1. Sectoral Water Use

Figures 3–6 show estimated sectoral water use at 0.1° globally over land excluding the Antarctic (~10km by ~10km at the equator). To our knowledge, this is the first time that water use for all sectors is estimated

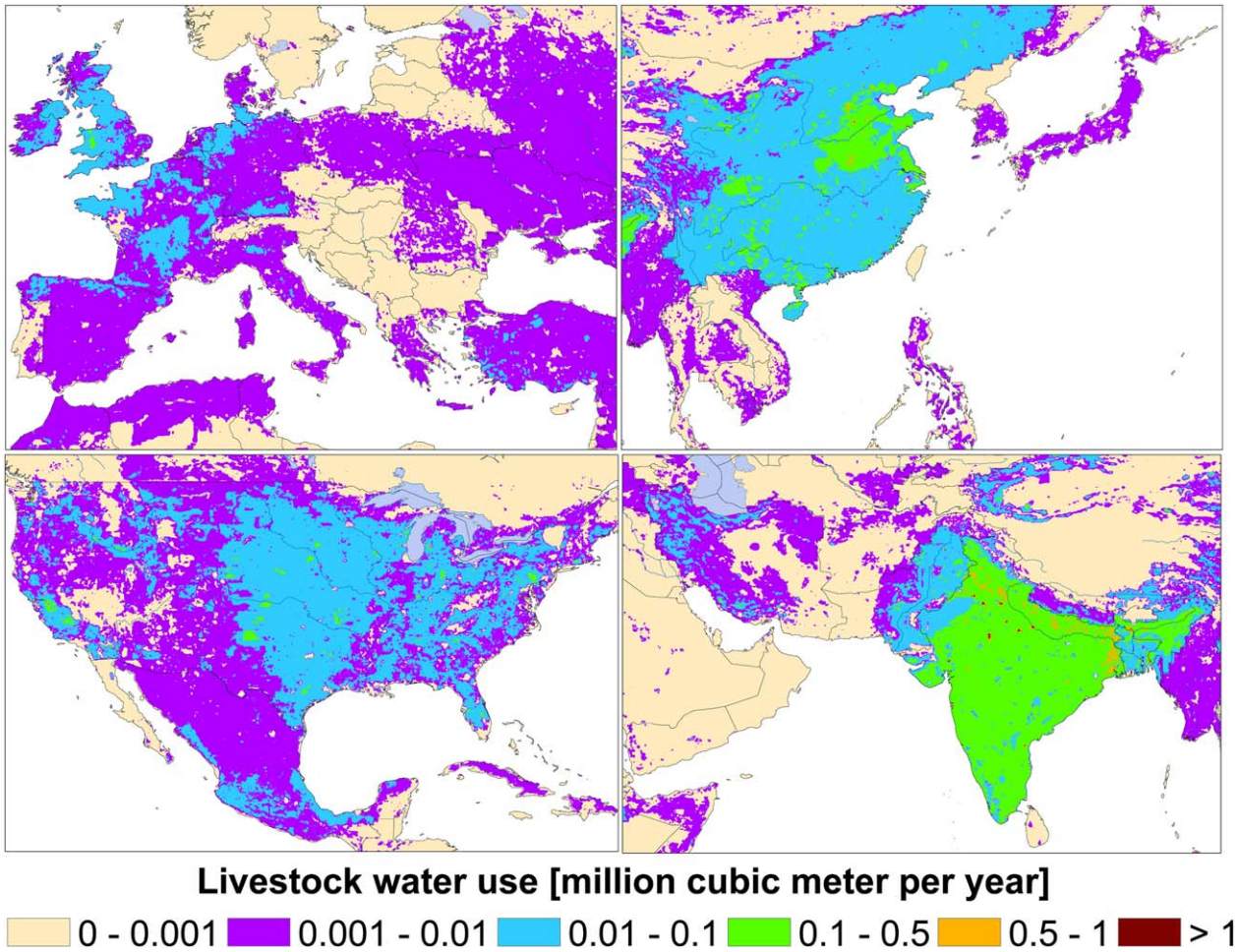

Figure 3. Livestock water use for the year 2010 at a 6 min spatial resolution. Global total equals 20 km^3 yr^{-1}.

globally at this spatial resolution. Compared to previously estimated water use at a 0.5° by 0.5° spatial scale (~50km by ~50km at the equator) [e.g., *Wada et al.*, 2014], detailed regional variations are clearly delineated at a 0.1° spatial scale. Higher spatial resolution also allows clearer distinction in land use pattern for agriculture (Figures 3 and 4). Due to much higher water use intensity, urban areas (e.g., New York, Paris, and Moscow) are noticeable at this scale (Figures 5 and 6). Figure 7 shows a time series estimate of global water use per sector. Over the period 1960–2010, livestock water use (consumption only) doubled from 10 to 20 km^3 yr^{-1}. Globally cattle accounts for 70% of the total. Buffaloes and sheep account for 10%, while goats, pigs and poultry share less than 5% of the total. Irrigation is a dominant water use sector (80%) and irrigation water use (withdrawal/consumption) has globally increased from 1300/650 to 2800/1400 km^3 yr^{-1} over the 50 years, respectively. Industrial and domestic water use (withdrawal/consumption) is growing rapidly (>300%) over the 50 years. Global total has increased from 350/120 to 950/300 km^3 yr^{-1} and from 90/60 to 450/200 km^3 yr^{-1} over the period, respectively. As a result, global total water use (withdrawal/consumption) has more than doubled (>250%) and exceeding 4000/1900 km^3 yr^{-1} for the year 2010, respectively. Water use is increasing particularly in India, Pakistan, China, West and Central United States, Mexico, South Europe, the Middle East and Central Asia (>50–100% over 1960–2010). More than 90% of the global irrigated areas are present in India, Pakistan, China, United States, Mexico, southern Europe, North Iran, and Nile delta. Increasing irrigation water use heightens our dependency on groundwater resources. Over the period 1960–2010, groundwater abstraction shows a consistent increase and nearly tripled from 350 km^3 yr^{-1} to 1000 km^3 yr^{-1}. For many developed countries (e.g., United States, Canada, Germany, France, Japan), rising water use is primarily driven by moderate but steady population growth and higher industrial activities (higher electricity and energy use).

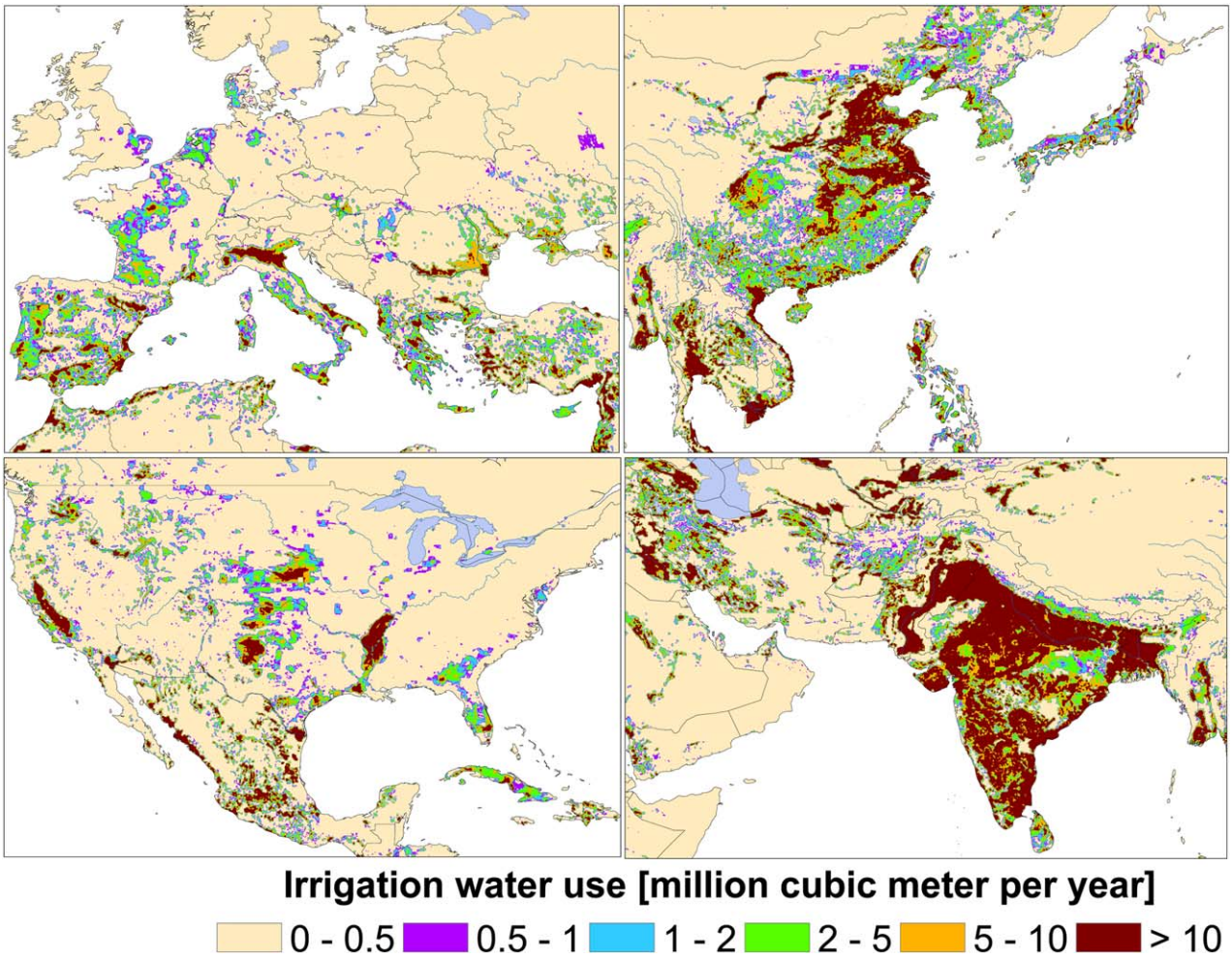

Figure 4. Irrigation water use for the year 2010 at a 6 min spatial resolution. Global total equals 2800 $km^3\ yr^{-1}$.

3.2. Human Impacts on Catchment Total Water Storage

Figure 8 compares for the period 2003–2010 the simulated monthly terrestrial water storage (TWS) anomalies with those from the GRACE observations [*Landerer and Swenson*, 2012] for a number of major river basins influenced at different extents by human activities. Simulated TWS has been derived from the sum of simulated snow, surface water, soil water, and groundwater storage. The TWS anomalies have been calculated over the overlapping period of 2003–2010 with the GRACE observation.

The comparison shows over all good agreement for the selected basins with the GRACE observations. In most basins, seasonal and inter-annual TWS signals have been altered by human activities. Human impacts on simulated TWS signals are particularly large over the Colorado, the Columbia, and the Indus basin, where the seasonal TWS amplitude slightly decreased, which is due to a combined effect of human water use and reservoir regulation. The peak TWS signals are reduced due to water extractions from surface water and groundwater storage, however, more water is released from reservoirs during the low flow period for water supply downstream. Including human activities in simulated TWS improves the correction (R^2) between the simulated and observed TWS from 0.77 to 0.82 (p-value < 0.0001) for the Columbia, but not for the Colorado and for the Indus where R^2 remains similar ($\sim$0.67, p value < 0.001, $\sim$0.52, p-value < 0.001, respectively). Over the Mississippi basin, dominant irrigation water use from groundwater and surface water decreases the peak TWS signals during the crop growing season. The correlation (R^2) improves from 0.76 to 0.80 (p value < 0.0001) for the Mississippi basin. For the Murray and the Parana basin, TWS is not well reproduced by our model simulation and the correlations are low ($R^2 < 0.5$). The error in climate forcing likely has a large impact on the poor performance, since the correlation is very high ($R^2 > 0.9$) before 2008 for the Murray.

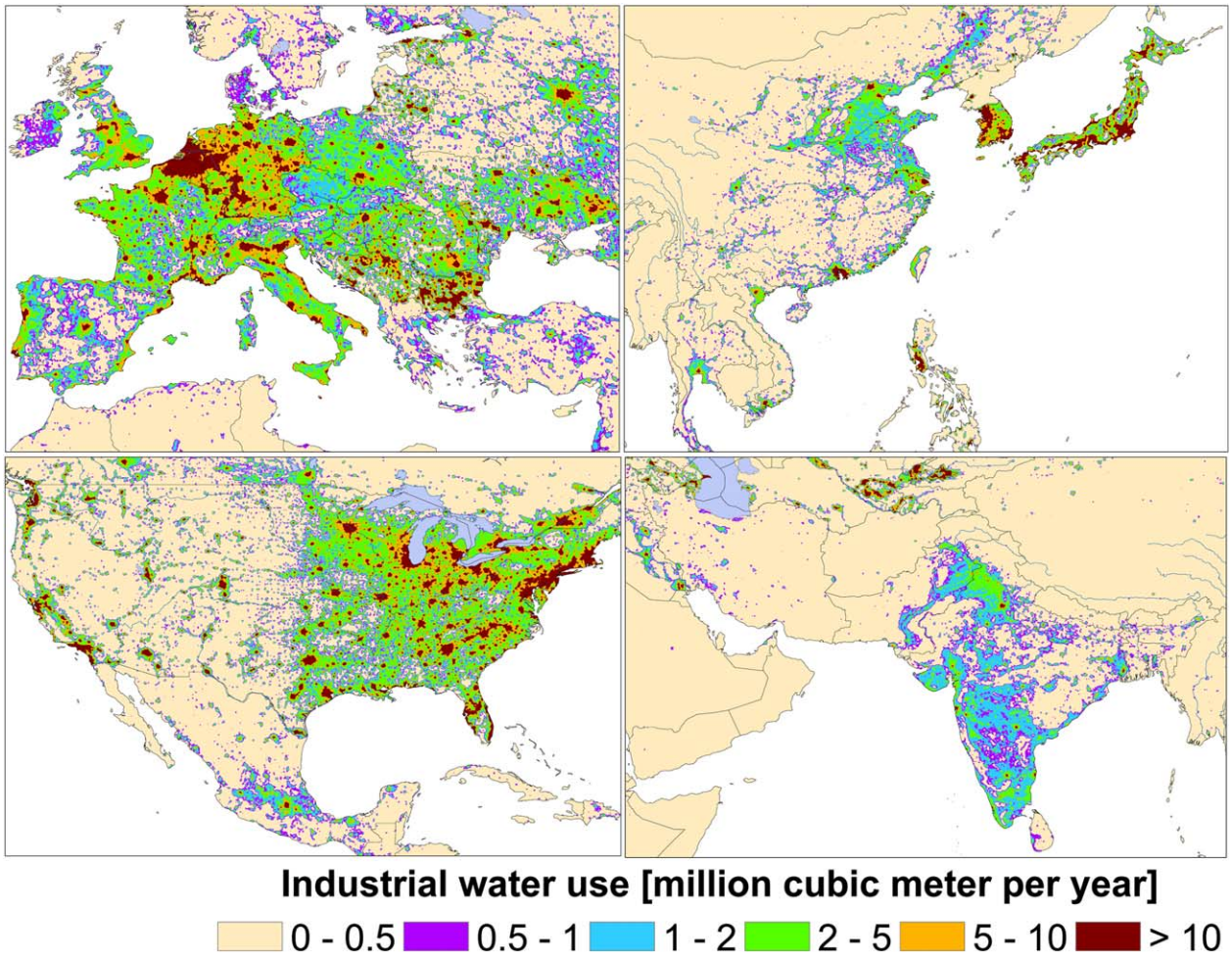

Figure 5. Industrial water use for the year 2010 at a 6 min spatial resolution. Global total equals 950 $km^3\ yr^{-1}$.

The impact of human activities is limited over these basins. For the Sao Francisco, the seasonal amplitude of TWS becomes larger when including human activities, primarily due to reservoir operations; however, the correlation becomes lower from 0.88 to 0.85. Our generic reservoir operation algorithm does not reproduce well regional reservoir management. Over the Rio Grande and the Rhine basin, human impacts are limited over simulated TWS and do not substantially change the correlation ($R^2 > \sim 0.75$, p value < 0.0001). Over the Ganges basin, similar to the Sao Francisco, human water use increases the seasonal amplitude of TWS change due to the fact that the low flow periods coincide with the growing season of irrigated crops (spring) which require large amounts of water. This improves R^2 from 0.85 to 0.90 (p value < 0.001) for the Ganges basin. Overall, model performance in TWS is adequate for most of the basins.

3.3. Multiscale Estimates of Regional Water Scarcity

In order to characterize the effect of spatial scales, water scarcity is estimated at three different spatial scales. Water scarcity is estimated with the ratio of water demand (Figures 3–6) to water availability (Figures 9 and 10; see also the river discharge validation in Tables 1 and 2): the so-called Water Stress Index [*Wada et al*., 2011a, 2011b]. The latter corresponds to the amount of water in rivers, lakes, reservoirs, and wetlands. Figure 11 shows estimated water stress calculated at a 0.1° grid. Fine regional variability in the magnitude of water stress is clearly delineated at this scale ($\sim$100km^2 at the equator), however, this approach underestimates total water availability in regions with extensive water supply network including large urban areas (e.g., Los Angeles, New York, London, Paris, and Moscow). Conventionally, water stress is calculated at a grid scale and a 0.5° grid ($\sim$2500 km^2 at the equator) is reasonably large enough to contain water supply network in those major cities. In Figure 12, water stress is estimated at the scale of subbain (so-called hydrobasin) in order to obtain more

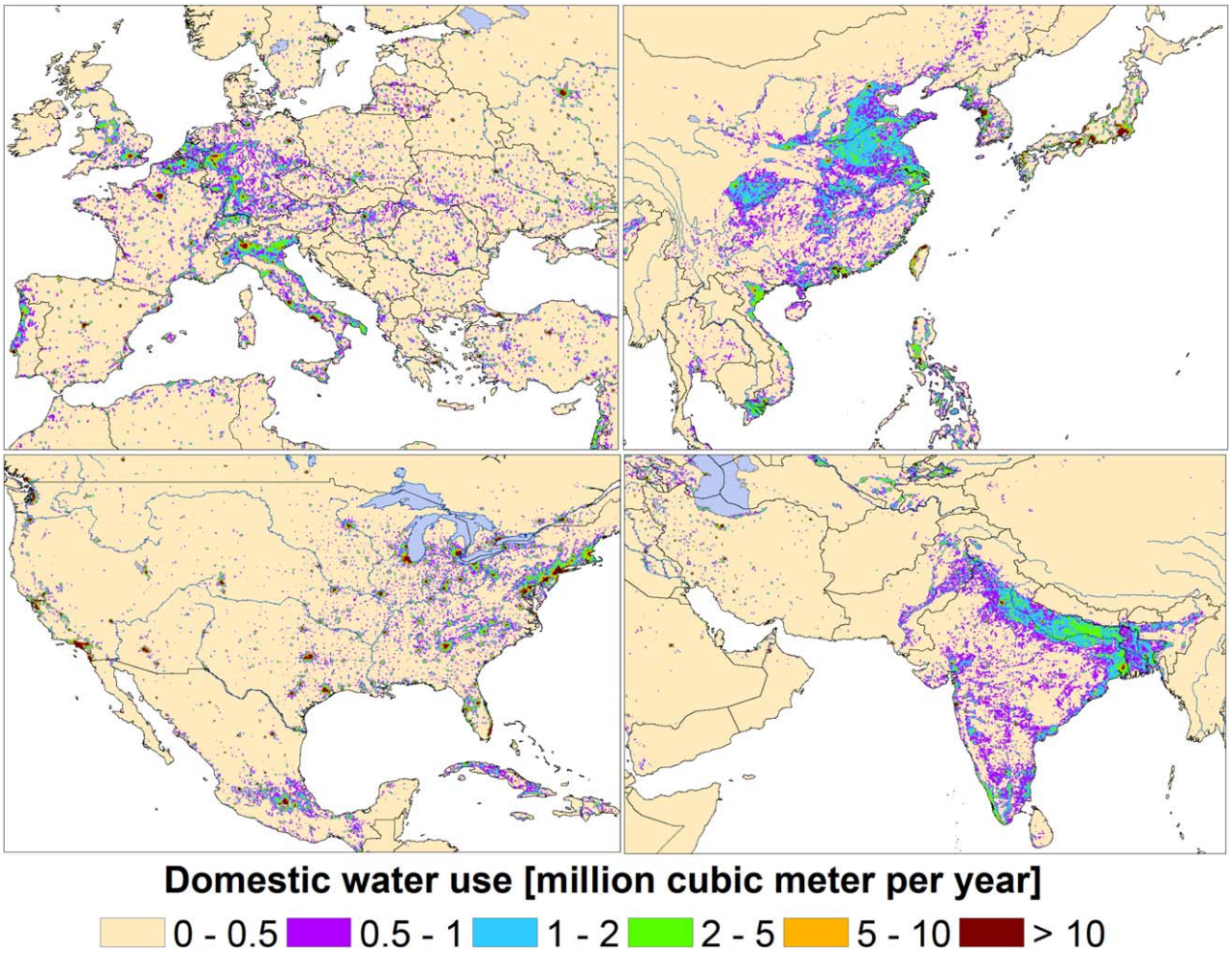

Figure 6. Domestic water use for the year 2010 at a 6 min spatial resolution. Global total equals 450 km^3 yr^{-1}.

accurate amount of water available to a region. This generally lowers the magnitude of water stress in many regions including urban areas. However, water stress remains high for irrigated areas with large water demand and limited surface water availability. Due to an aggregation of grid cells, this approach overestimates water stress for many local areas, i.e., part of large hydrobasins (e.g., the Indus, Saudi Arabia, Iran, Western China, and

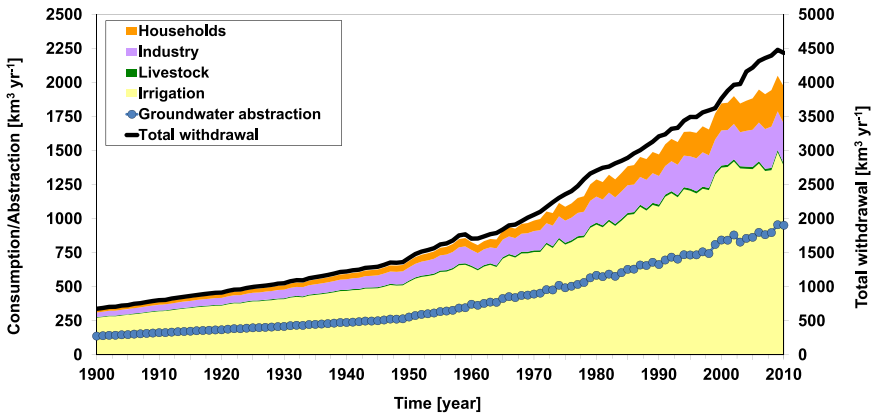

Figure 7. Global sectoral water use and groundwater abstraction over the period 1900–2010. The model simulation was done from 1960 onward, but earlier results were obtained from *Wada et al.* [2012b].

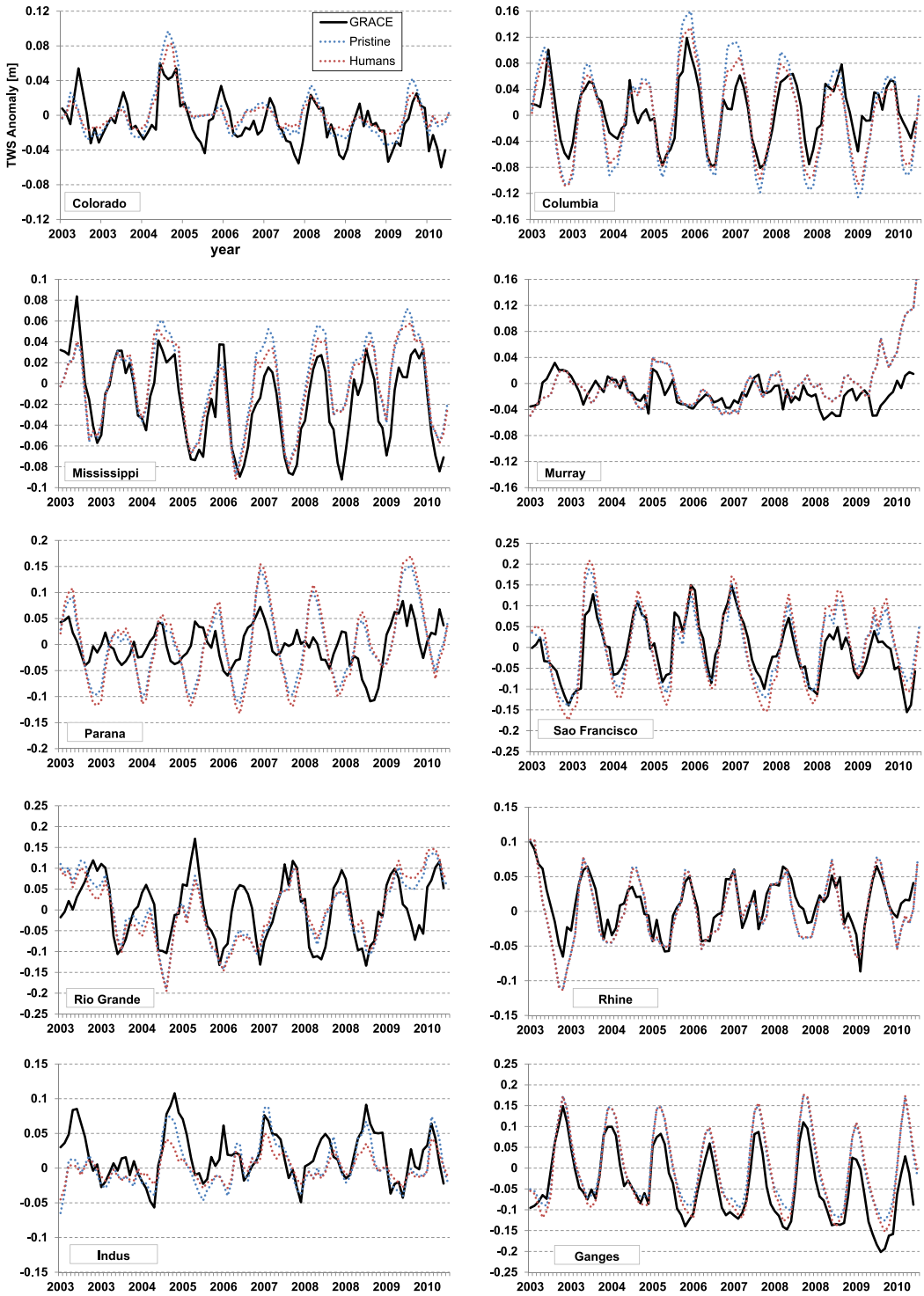

Figure 8. Comparison of simulated TWS under the pristine condition (pristine; blue) and under human influences (humans; red) to observed TWS derived from GRACE observation data (black). TWS anomaly is calculated over the period 2003–2010 (unit: meter).

Central Asia). Water stress is then calculated at the scale of small administrative unit (i.e., county) where regional water supply network is generally managed (Figure 13). The result shows distinct pattern of water stress and the magnitude of water stress generally becomes much lower for many regions. It should be noted that in many regions single water supply network is managed not as extensive as county-scale so water availability is likely overestimated at this scale.

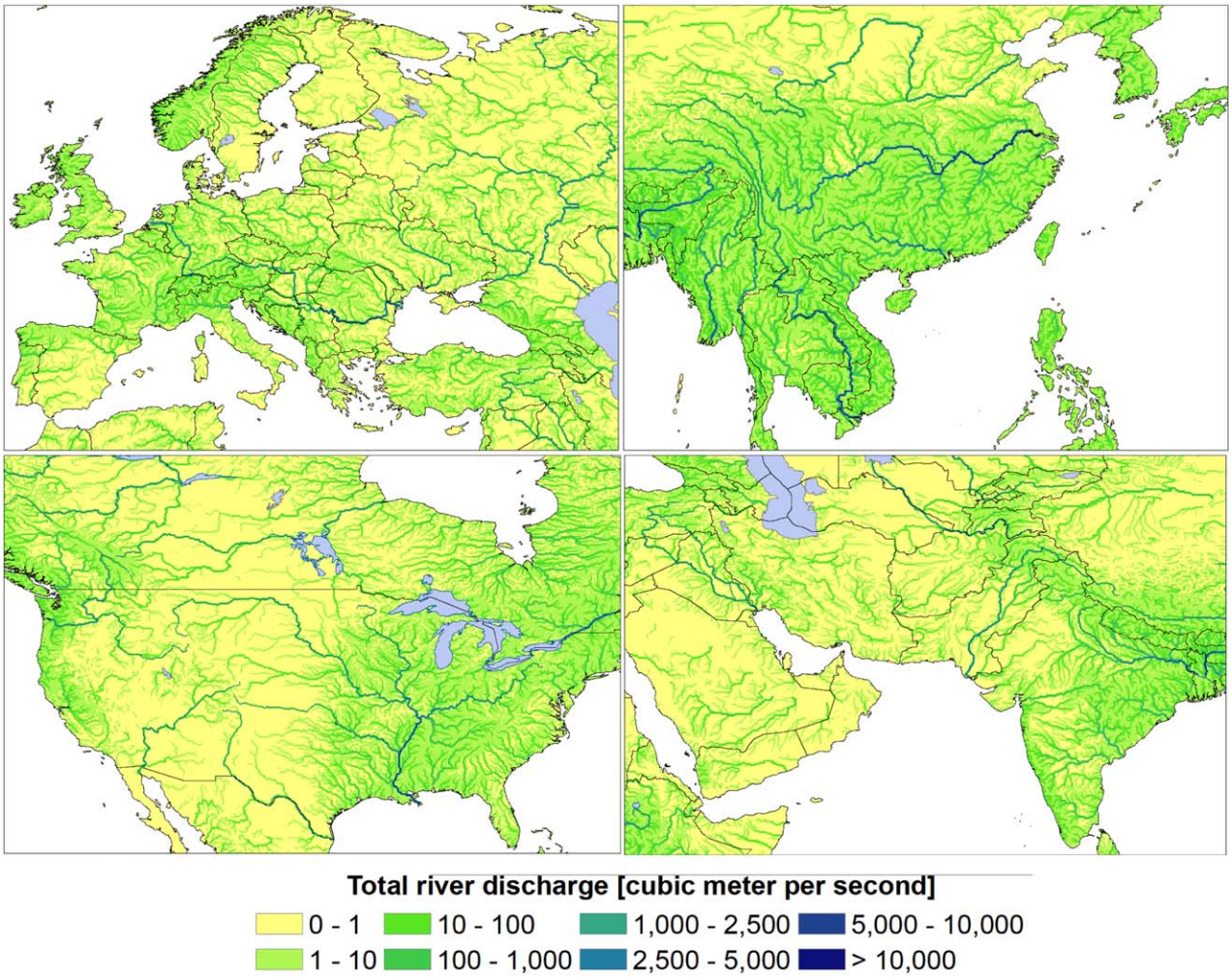

Figure 9. Simulated average total river discharge in the Northern Hemisphere for the period 1960–2010.

3.4. Human Impacts on Groundwater Resources

3.4.1. Groundwater Depths and Evaluation

Figure 14 shows the steady-state simulated groundwater table depths (meters below the land-surface) under the natural conditions. General patterns in water table depths can be identified. Throughout the entire coastal ribbon shallow groundwater tables occur (as the sea level acts as a constant head boundary condition) and these areas expand where flat coastal plains meet the sea, e.g., for the Mississippi, Indus, and Ganges. At the regional scale, recharge is the main control together with regional scale topography. Regions with high recharge rates have shallow groundwater tables, e.g., the tropical swaps of the Amazon. The influence of the regional scale topography is evident, e.g., for the central Amazon and the flat lowlands of South America, as these regions receive water from elevated areas. Regions with low recharge rates show deep groundwater tables where groundwater gets disconnected from the local drainage. The deserts stand out. Also, deep groundwater tables are simulated for the mountain ranges. For these regions the deeper regional scale groundwater table is simulated (illustrated in Figure 14), and local valleys in the mountain ranges with local shallow groundwater tables are likely underestimated due to the grid resolution. The mountain regions where perched water tables are likely to occur are masked with a transparent layer in Figure 14.

3.4.2. Groundwater Base Flow Change

The ratio of groundwater base flow to recharge is calculated for the regional scale aquifers of the world for the pristine and human scenarios. The histogram of Figure 15 gives the global distribution, the maps show the spatial distribution of the ratio for North-America. When the ratio is 1, all water going in also goes out within the

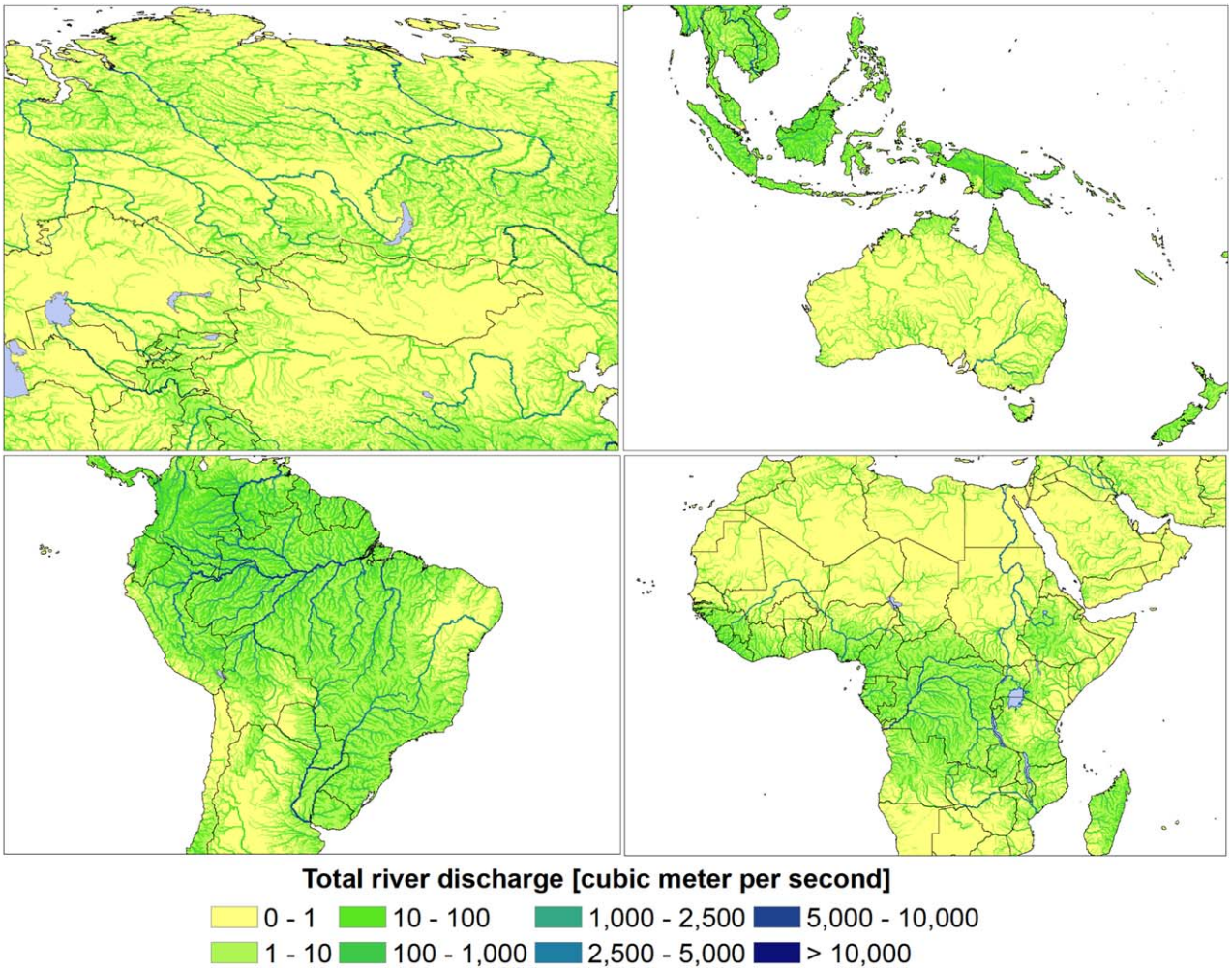

Figure 10. Simulated average total river discharge in the Eurasia and the Southern Hemisphere for the period 1960–2010.

same aquifer. The largest deviations can be found for regions with little recharge. Due to abstractions, less groundwater will leave the aquifer as discharge and ratios get smaller. This is seen in the histogram, and also for example over the High Plain aquifer that shows very low ratios when abstractions are included. This shift shows the effects of groundwater abstractions can be huge, especially for intensively pumped aquifers with abstractions exceeding recharge by many times. For these areas base flow magnitudes to rivers decrease, and maintenance of base flows during droughts is mostly likely not secured and critical river flows needed to maintain valuable ecosystems are not adequately sustained. The terms importing and exporting refer to the pristine-run, where groundwater is imported from upstream catchments when more water is drained than recharged and exported to downstream aquifers when less water is drained than recharged. However, in the human-run extra water is leaving the aquifer by abstractions and not via more inter-basin groundwater flow at the aquifer scale. The bottom figure shows aquifers that shifted from importing groundwater to "exporting" groundwater. This shows groundwater pathways and lengths are changed due to abstractions from higher elevated aquifers. No aquifers exist with a shift from exporting to importing groundwater worldwide.

3.5. Groundwater Depletion

Since the effect of groundwater pumping is most obvious at local scales and the impact of overexploitation is highly localized, groundwater depletion is estimated at a 0.1° grid scale (Figure 16). Groundwater depletion (the year 2010) is calculated from the difference between groundwater abstraction (the year 2010) (Figure 17) and groundwater recharge (average 1960–2010) (Figure 18). Here groundwater recharge includes natural groundwater recharge from precipitation (16,500 km^3 yr^{-1}) return flow from irrigation (1200 km^3

Table 1. Comparison of Simulated to Observed River Discharge Under the Natural Conditions (N) and Under Human-Induced Change (Water Use and Reservoir Regulation) (H) for Major Basins of the World[a]

	Monthly Statistics						Annual Statistics					
	R^2		α		*NSC*		R^2		α		*NSC*	
River Basin	N	H	N	H	N	H	N	H	N	H	N	H
Amazon	0.98	0.98	1.06	1.06	0.57	0.58	1.00	1.00	1.02	1.02	0.29	0.29
Orinoco	0.97	0.98	0.96	1.01	0.66	0.77	0.99	0.99	1.01	1.01	0.67	0.77
Parana	0.88	0.94	0.74	0.77	−2.05	−0.54	0.99	0.98	0.78	0.89	0.08	0.10
Congo	0.94	0.98	0.82	0.84	−1.44	−1.12	1.00	1.00	0.87	0.87	−0.62	−0.64
Nile	0.79	0.79	0.26	0.32	<−10	<−10	0.98	0.99	0.29	0.37	<−10	<−10
Blue Nile	0.75	0.77	0.66	0.71	0.02	0.04	0.97	0.98	0.73	0.71	−2.80	−2.30
White Nile	0.9	0.92	0.35	0.40	−8.8	−8.6	0.98	0.99	0.48	0.49	−7.5	−7.2
Niger	0.63	0.6	0.49	0.50	−9.06	−8.7	1.00	0.99	0.54	0.53	−8.2	−8.0
Orange	0.66	0.8	0.58	0.66	0.2	0.32	0.81	0.86	0.65	0.77	−4.37	−4.19
Zambezi	0.73	0.82	0.53	0.54	−1.26	−1.2	0.99	0.97	0.67	0.66	−0.54	−0.53
Murray	0.7	0.86	0.59	0.62	0.19	0.27	0.88	0.96	0.66	0.75	−3.89	−2.86
Mekong	0.94	0.98	1.13	1.08	0.7	0.74	0.99	1.00	1.08	1.06	0.43	0.52
Brahmaputra	0.8	0.85	1.19	1.20	0.67	0.68	1.00	0.99	1.12	1.11	0.40	0.42
Ganges	0.86	0.89	1.08	1.04	0.73	0.76	1.00	1.00	1.09	1.04	0.71	0.90
Indus	0.75	0.76	0.88	0.96	0.19	0.4	0.97	0.99	0.90	0.97	−0.88	0.13
Yangtze	0.93	0.96	1.17	1.11	0.64	0.66	0.99	1.00	1.11	1.06	0.72	0.82
Huang He	0.79	0.73	0.87	0.78	0.28	0.56	0.95	0.97	0.92	0.85	−0.53	−1.94
Mississippi	0.86	0.93	0.93	1.07	0.61	0.65	0.99	1.00	0.99	1.01	0.82	0.90
Columbia	0.96	0.98	0.93	1.04	0.47	0.52	0.98	1.00	0.98	1.02	0.30	0.55
Mckenzie	0.72	0.74	1.33	1.29	0.35	0.38	0.98	0.98	1.11	1.13	0.18	0.22
Lena	0.8	0.8	1.19	1.19	0.62	0.56	1.00	1.00	1.01	1.01	0.80	0.85
Volga	0.76	0.8	0.95	1.04	0.66	0.68	1.00	1.00	0.93	1.04	0.69	0.75
Dnieper	0.82	0.84	0.80	0.87	0.2	0.25	0.99	1.00	0.87	0.94	−0.93	−1.26
Danube	0.97	0.98	0.84	0.92	0.56	0.65	0.98	0.99	0.89	0.97	0.40	0.46
Rhine	0.95	0.98	0.95	0.97	0.78	0.82	0.99	1.00	1.02	1.03	0.90	0.92
Elbe	0.88	0.92	0.73	0.77	−0.68	−0.24	0.98	1.00	0.80	0.88	−0.21	−0.02

[a]The observed river discharge has been taken from the selected GRDC stations closest to outlets based on available records (1960–2010) for each basin. R^2, α, and *NSC* denote the coefficient of determination, the slope (x-coordinate: simulated discharge; y-coordinate: observed discharge), and the Nash-Sutcliffe model efficiency coefficient.

yr^{-1}) and return flow from the industrial and domestic sectors (300 km^3 yr^{-1}). In addition, original groundwater depletion estimates have been corrected by using a multiplicative correction factor per climate zone based on aridity (hyper-arid to humid) in order to compensate for increased capture of discharge and enhance recharge due to pumping that may be significant over semi-arid to sub-humid climate zones. The correction factors have been derived from a comparison between original depletion estimates to independent regional estimates of groundwater depletion based on *Wada et al*. [2012b]. After the correction, global groundwater depletion estimates become 120 km^3 yr^{-1} (originally from 200 km^3 yr^{-1}). Groundwater depletion is substantial over India, Northeast China, United States, Pakistan, South Europe, South Mexico, North Iran and Central Saudi Arabia, where irrigation contributes more than 90% to the depletion. Summing groundwater depletion over these regions amounts to 90% of the global total. Note that we did not use the groundwater model yet to estimate groundwater depletion. This is mainly because vertical structure of the aquifers that holds crucial information about accessibility of the groundwater is missing in the used aquifer parameterization.

4. Validation

4.1. Accuracy of High-Resolution Simulation Results

In order to evaluate the effect of human impacts on surface water and groundwater resources, we compare simulation results to available observations and statistics. We focus on validating simulated river discharges, groundwater heads, and sectoral water use. Observed river discharges are available per gauging stations from the Global Runoff Data Centre; http://www.bafg.de/GRDC/). In earlier work, our modeling approaches at a 0.5° spatial resolution were extensively validated and showed good agreement with observations for most regions of the world: simulated runoff and river discharge (average, minimum and maximum) against GRDC observations [*Van Beek et al*., 2011], simulated actual evapotranspiration against the ERA-40 reanalysis data [*Van Beek et al*., 2011], simulated total terrestrial water storage (TWS) against the GRACE satellite

Table 2. Comparison of Average, Minimum (Low), and Maximum (Peak) Streamflow Derived From Observed (O) and Simulated Streamflow Under the Natural Conditions (N) and Under Human-Induced Change (Water Use and Reservoir Regulation) (H) for Major Basins of the World[a]

	Qavg							Qmin							Qmax						
	Streamflow ($m^3 s^{-1}$)			R^2		*NSC*		Streamflow ($m^3 s^{-1}$)			R^2		*NSC*		Streamflow ($m^3 s^{-1}$)			R^2		*NSC*	
River Basin	O	N	N	N	H	N	H	O	N	H	N	H	N	H	O	N	H	N	H	N	H
Amazon	176,418	165,230	168,689	0.98	0.98	0.57	0.58	69,271	63,570	63,206	0.75	0.77	0.41	0.41	306,345	279,807	265,419	0.83	0.84	0.35	0.34
Orinoco	31,206	31,651	32,122	0.97	0.98	0.66	0.77	4,359	8,056	6,825	0.57	0.61	0.48	0.55	85,964	80,654	77,953	0.82	0.85	0.38	0.39
Parana	16,595	22,267	21,757	0.88	0.94	−2.05	−0.54	6,108	6,909	6,810	0.70	0.76	0.09	0.21	54,500	49,723	49,704	0.90	0.93	0.07	0.08
Congo	40,251	44,806	44,335	0.94	0.98	−1.44	−1.12	24,360	30,283	26,127	0.73	0.74	−0.29	−0.25	80,833	90,825	84,782	0.81	0.81	−0.07	−0.07
Nile	1,251	7,726	6,562	0.79	0.79	<−10	<−10	735	2,764	823	0.62	0.66	<−10	0.55	5,850	15,016	11,554	0.12	0.12	−8.24	−7.65
Blue Nile	1,513	2,767	2,426	0.75	0.77	0.02	0.04	50	1,295	913	0.54	0.72	0.02	0.12	7,205	9,353	8,600	0.53	0.54	0.02	0.02
White Nile	939	4,072	3,836	0.90	0.92	−8.8	−8.6	509	1,863	1,188	0.46	0.71	−5.71	0.12	2,396	12,176	12,185	0.37	0.39	<−10	<−10
Niger	887	2,529	2,343	0.63	0.60	−9.06	−8.7	3	248	0	0.21	0.86	−4.61	0.34	12,314	16,599	15,527	0.65	0.66	0.29	0.3
Orange	286	803	610	0.66	0.80	0.20	0.32	1	251	13	0.23	0.84	−2.05	0.27	4,458	3,943	3,438	0.77	0.76	0.33	0.21
Zambezi	1,169	2,040	1,970	0.73	0.82	−1.26	−1.2	146	290	56	0.65	0.78	0.08	0.12	7,352	8,935	8,428	0.84	0.88	0.59	0.6
Murray	9	59	32	0.70	0.86	0.19	0.27	0	25	1	0.47	0.82	0.01	0.08	176	449	244	0.39	0.69	0.01	0.42
Mekong	7,968	8,390	7,733	0.94	0.98	0.70	0.74	1,045	1,560	1,117	0.78	0.85	0.66	0.72	32,953	28,029	29,031	0.61	0.73	0.52	0.67
Brahmaputra	21,112	18,892	18,284	0.80	0.85	0.67	0.68	3,314	3,946	3,523	0.74	0.76	0.53	0.65	59,326	48,362	47,826	0.61	0.64	0.48	0.52
Ganges	12,037	11,149	9,539	0.86	0.89	0.73	0.76	1,181	1,361	742	0.74	0.72	0.59	0.61	65,072	51,451	54,022	0.60	0.59	0.50	0.47
Indus	2,904	3,556	2,156	0.75	0.76	0.19	0.4	208	565	92	0.53	0.75	0.15	0.39	22,500	19,300	16,071	0.83	0.64	0.32	−0.28
Yangtze	28,521	23,975	24,483	0.93	0.96	0.64	0.66	1,110	6,690	3,705	0.25	0.48	−2.87	0.21	84,200	68,060	67,303	0.61	0.61	−2.37	−1.2
Huang He	1,261	1,828	1,279	0.79	0.73	0.28	0.56	96	388	59	0.28	0.72	−2.97	0.32	5,340	5,575	5,393	0.93	0.94	0.63	0.88
Mississippi	17,150	18,671	17,108	0.86	0.93	0.61	0.65	4,221	5,684	4,862	0.73	0.78	0.61	0.65	55,056	46,288	45,252	0.79	0.77	0.50	0.46
Columbia	5,371	5,500	5,215	0.96	0.98	0.47	0.52	2,145	2,213	1,838	0.74	0.78	0.38	0.51	16,738	12,346	12,434	0.80	0.75	0.40	0.35
Mckenzie	9,477	7,646	8,055	0.72	0.74	0.35	0.38	2,132	3,272	2,876	0.68	0.77	0.12	0.32	24,742	19,016	18,483	0.56	0.65	0.20	0.18
Lena	16,704	17,941	17,782	0.80	0.80	0.62	0.56	721	3,317	3,463	0.43	0.46	0.51	0.54	103,830	86,327	90,002	0.79	0.81	0.44	0.47
Volga	8,141	8,382	8,016	0.76	0.80	0.66	0.68	3,165	2,793	2,730	0.72	0.78	0.50	0.55	39,400	30,109	28,127	0.61	0.61	0.44	0.46
Dnieper	1,492	1,874	1,643	0.82	0.84	0.20	0.25	434	653	217	0.62	0.85	0.19	0.34	6,830	6,902	6,451	0.97	0.98	0.79	0.88
Danube	6,415	7,590	6,947	0.97	0.98	0.56	0.65	2,338	3,153	2,434	0.74	0.72	0.45	0.52	14,518	17,473	16,362	0.67	0.72	0.38	0.46
Rhine	2,253	2,547	2,341	0.95	0.98	0.78	0.82	820	1,003	756	0.74	0.86	0.71	0.64	7,279	5,816	6,099	0.71	0.73	0.68	0.59
Elbe	680	852	740	0.88	0.92	−0.68	−0.24	218	393	210	0.66	0.81	0.14	0.42	2,345	2,715	2,532	0.86	0.96	0.65	0.87

[a]The observed streamflow has been taken from the selected GRDC stations with the longest available records (N>120; 1960–2010) for each basin. R^2 (the coefficient of determination) and *NSC* [*Nash and Sutcliffe*, 1970] have been calculated from comparison between observed and simulated monthly streamflow.

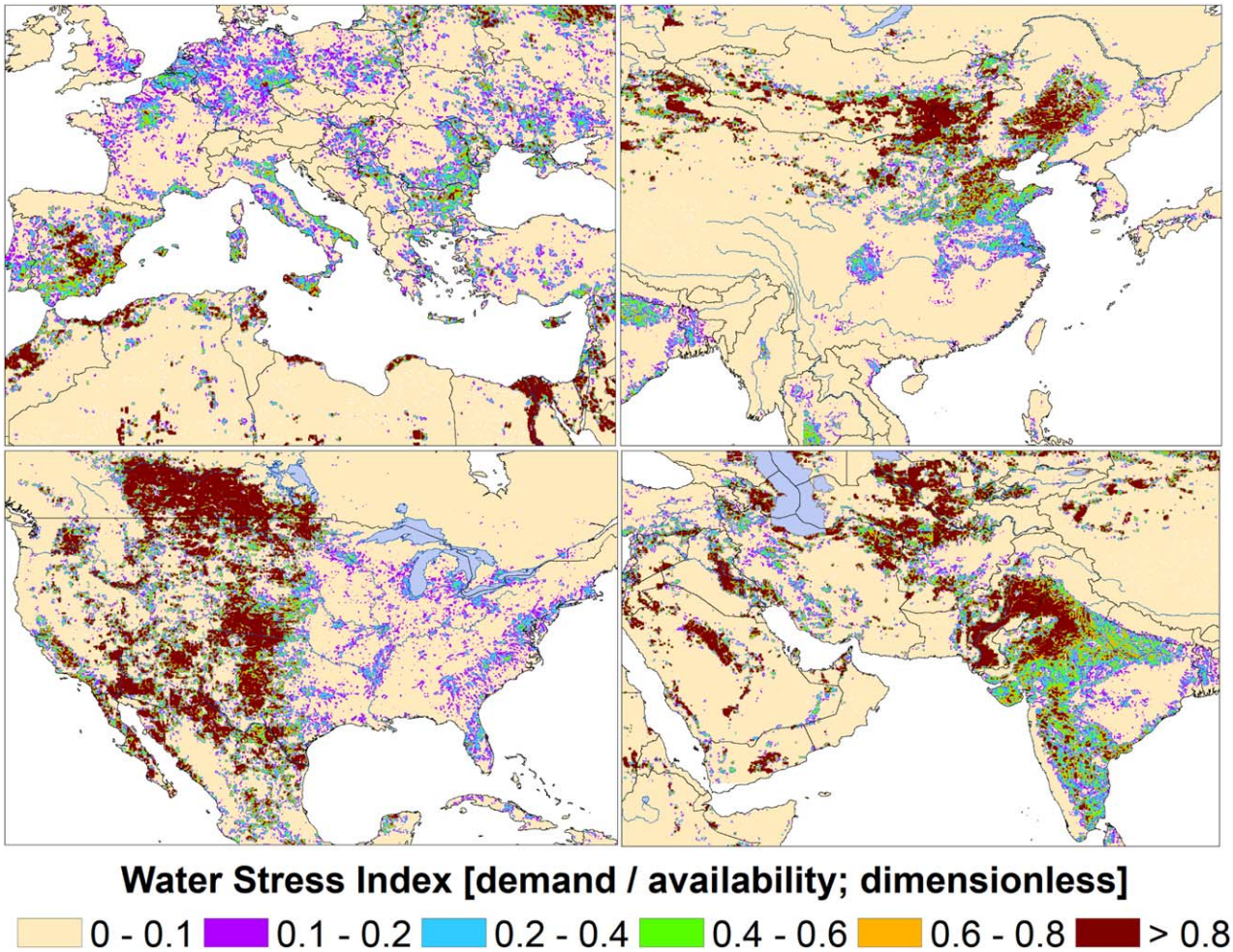

Figure 11. Water Stress Index for 2010 calculated at a 6 min spatial resolution.

observations [*Wada et al*., 2012a, 2014], simulated low-flow or drought characteristics against GRDC observations [*Wada et al*., 2013], estimated sectoral water withdrawal and consumption for livestock, irrigation, industry and households against the FAO AQUASTAT database and *Shiklomanov* [2000a, 2000b] [*Wada et al*., 2011a], simulated water use per sector per source (surface water and groundwater) against the FAO AQUASTAT database, the Eurostat database (http://epp.eurostat.ec.europa.eu/), the U. S. Geological Survey (http://water.usgs.gov/watuse/) and other national and sub-national statistics including India, China and Mexico [*Wada and Heinrich*, 2013; *Wada et al*., 2014], and simulated water scarcity against country drought statistics and historical observation [*Wada et al*., 2011a, 2011b]. Water use statistics are typically available at a scale of country or state/province, and improvement in spatial resolution of simulated results can hardly be validated at the corresponding spatial resolution of our high-resolution modeling framework (~0.1°).

4.2. Comparison of Simulated to Observed Maximum, Average, and Minimum Discharges

In order to estimate accurate seasonal water availability per region, it is vital to have a correct estimate of the flow duration curve, i.e., minimum and maximum flow. When peak flow is poorly reproduced, there is likely a considerable mismatch in simulating low flow events. In Tables 1 and 2, we evaluate simulated annual and monthly streamflow against available GRDC stations. We consider simulated streamflow both under pristine conditions and under human influences, and compare average, minimum (low), and maximum (peak) streamflow derived from observed and simulated monthly streamflow. For the comparisons, we have selected major basins of the world that cover a wide range of climate and human impacts including reservoir regulation. Our simulated streamflow is generally comparable to observed streamflow for most of the basins, where R^2 is over 0.9 except for the Elbe and Zambezi, and *NSC* (Nash-Sutcliffe model

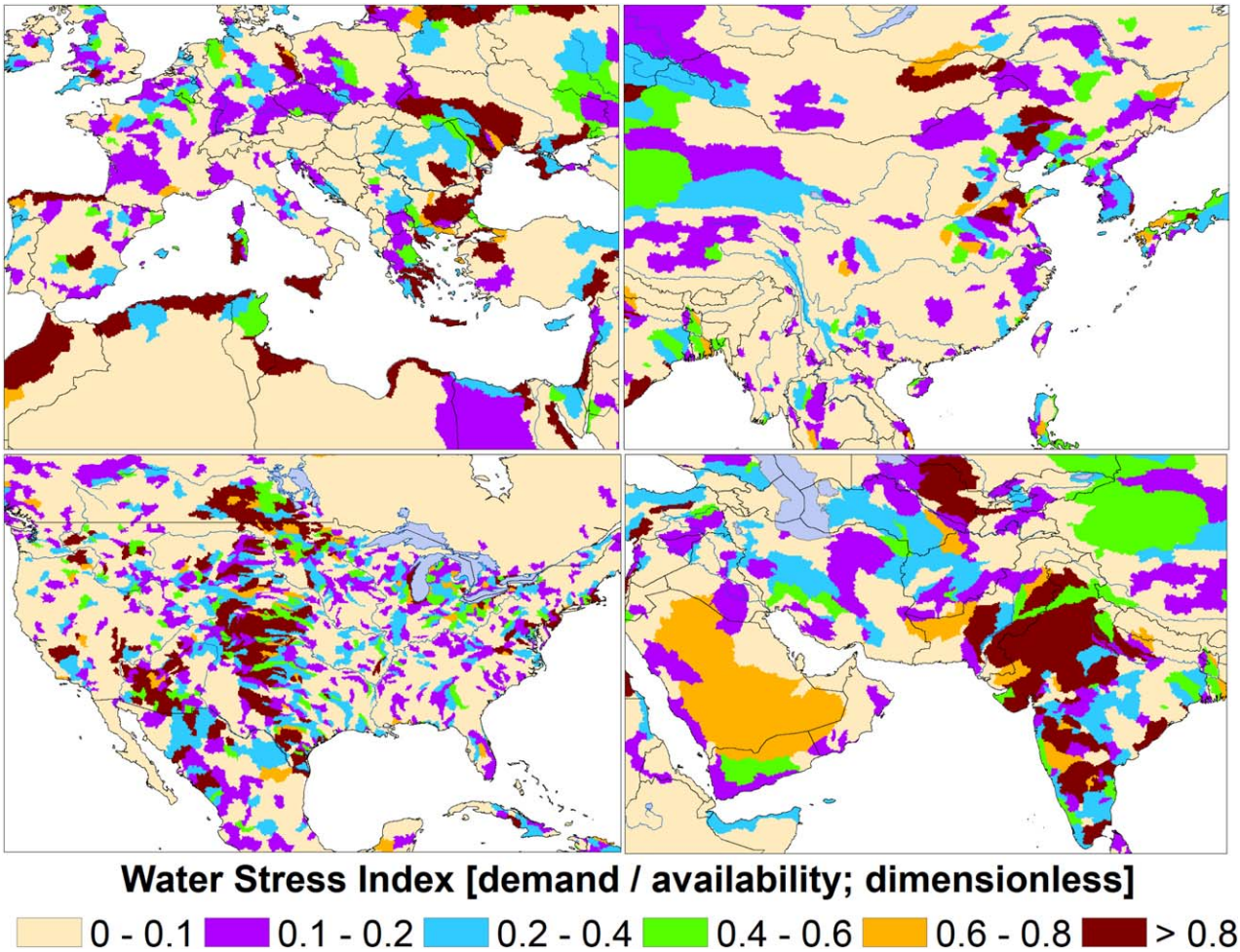

Figure 12. Water Stress Index for 2010 calculated over hydrobasins or subbasins. The subbasin data set was obtained from the FAO AQUASTAT database (http://www.fao.org/nr/water/aquastat/main/index.stm/) that used the HydroSHEDS to derive the subbasins.

efficiency coefficient) is over 0.6 except for the Elbe, Congo, and Zambezi. The effect of water consumption is clearly observable for the rivers crossing major irrigated areas of the world with the number of existing reservoirs including the Nile, the Orange, the Murray, the Mekong, the Ganges, the Indus, the Yangtze, the Huang He, the Mississippi, the Columbia, and the Volga. For the other river basins, the impact of water consumption is less obvious, but still noticeable such as for the Orinoco, the Parana, the Brahmaputra, the Danube, the Rhine, the Dnieper, and the Elbe. For the Amazon, the Congo, the Niger, the Zambezi, the Mckenzie, and the Lena, the river discharge is hardly affected because of lower water consumption. For those river basins where water consumption is large including the Orinoco, Parana, Mississippi, Rhine, Danube, Mekong, and Yangtze, the overall model performance (R^2: the coefficient-of-determination, α: slope or regression coefficient, *NSC*: the Nash-Sutcliffe model efficiency coefficient) improves when considering water consumption, except for the Ganges and the Huang He where our general model performance is low. This improvement is particularly evident for simulated minimum streamflow and for river basins where the low flow periods coincide with the large seasonal water demands, e.g., the growing season of irrigated crops (e.g., Orange, Murray, Brahmaputra, Indus, and Huang He). For the Elbe, Congo, and Zambezi, water consumption has little influence on simulated discharges. When including all available GRDC stations with long streamflow records (Table 3), the comparison of observed and simulated streamflow also shows improved performance when including water consumption, but the maximum (peak) streamflow is hardly affected. Overall, the correlation between the simulated and the observed river discharge is high for most of the river basins, while the Nash-Sutcliffe model efficiency coefficient is high for some river basins but low

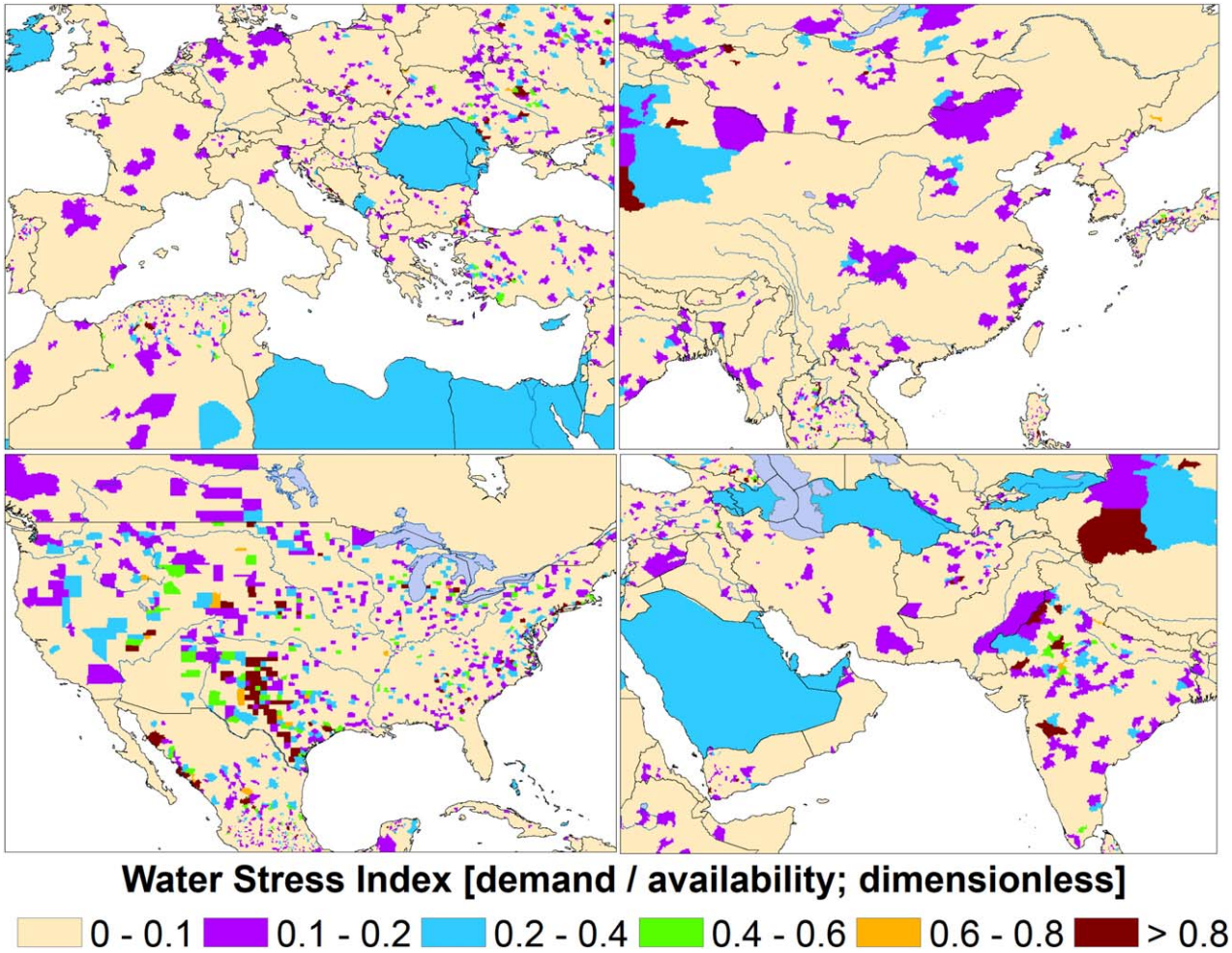

Figure 13. Water Stress Index for 2010 calculated over county-scale administrative units. Note county-scale information is not available in some countries.

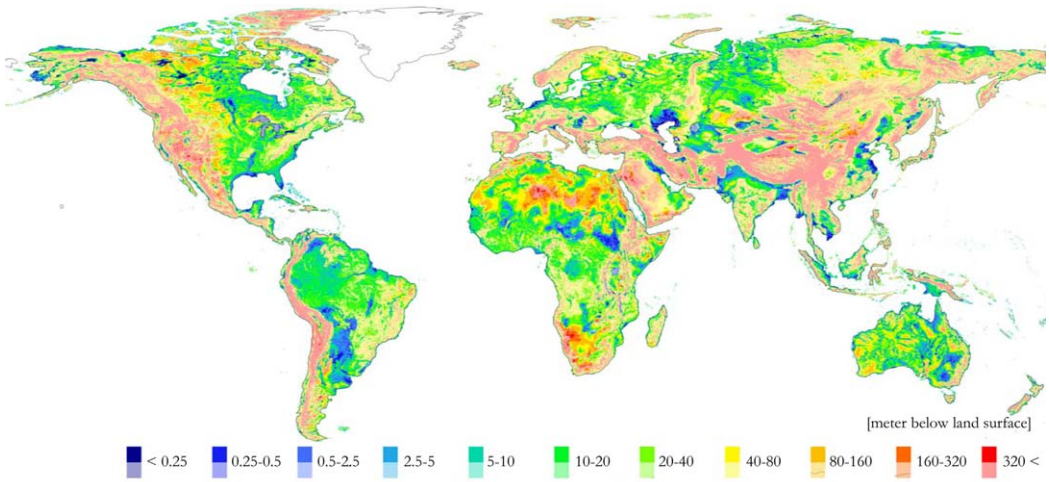

Figure 14. Simulated groundwater depths for the natural steady state.

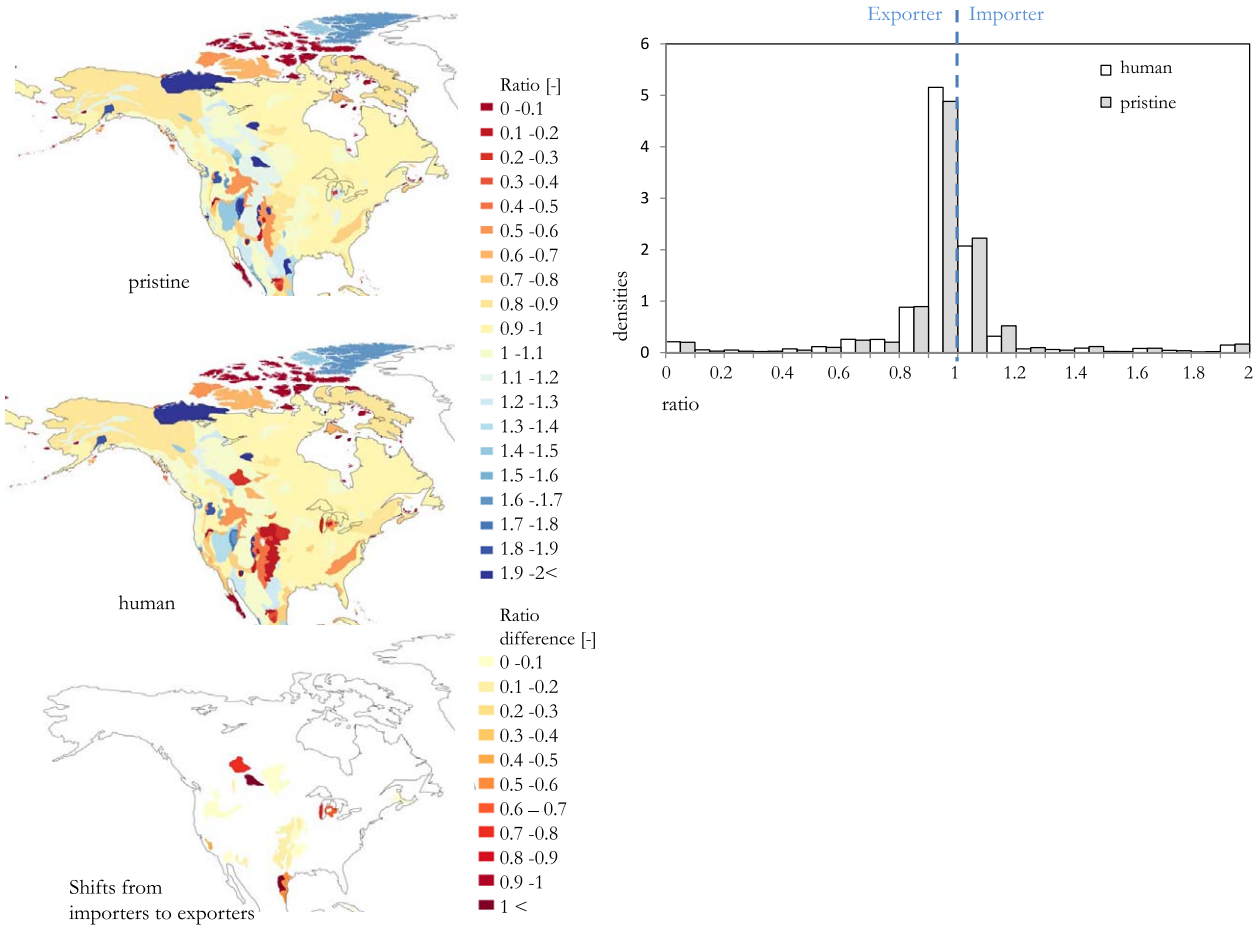

Figure 15. (left) Groundwater discharge – recharge ratio, zoomed for North America, and shifts in importer to exporter. (right) Histogram of the ratio, globally. Exporting and importing refers to the pristine situation, where if less water is drained than recharged water is exported from the aquifer via lateral flows, if more water is drained than recharged water is imported via lateral flows. For the "human-run" this terminology is somewhat misleading, as the ratio becomes mainly smaller due to the abstractions and not by more exported groundwater. Still, the smaller fraction illustrates a decline in groundwater flow to the local drainage within the aquifer. The bottom figure shows the shift from importers to "exporters."

for several basins including the Nile, the Niger, and the Orange where the number of observational records are limited.

4.3. Comparison of Simulated to Observed Groundwater Heads

Simulated groundwater heads of both runs (pristine and human) have been evaluated against measured data [*Fan et al.*, 2013]. The average of the reported data has been used if more than one observation is available within a grid cell (0.1°), giving a total of 65,303 cells with observations worldwide (of the total 6,480,000 cells). For most regions of the world no observational data are available or are incomplete. While interpreting the results, note that observations are biased toward river valleys, coastal ribbons, and areas with productive aquifers. Also, observations are taken at a certain moment in time, and thus are susceptible to seasonal effects and drawdown as a result of abstraction, while simulated results are steady-state. Besides, it is likely that for mountain ranges perched water tables are sampled instead of the deeper regional scale. As stated before, the regional scale groundwater table is simulated as the result of grid resolution. The scatter plot of Figure 19 shows observed heads against simulated heads for the pristine run. Statistics of both runs, R^2 (coefficient of determination) and α (regression coefficient) are given. The scatter shows that model performance is good. However, is shows a strong underestimation, meaning that simulated groundwater heads are too deep. This underestimation occurs for higher elevated areas, where shallow local water tables are sampled but the deeper regional scale groundwater table is simulated [*de Graaf et al.*, 2015]. Therefore, we evaluated R^2 and α for mountain ranges and sediment basins separately. The

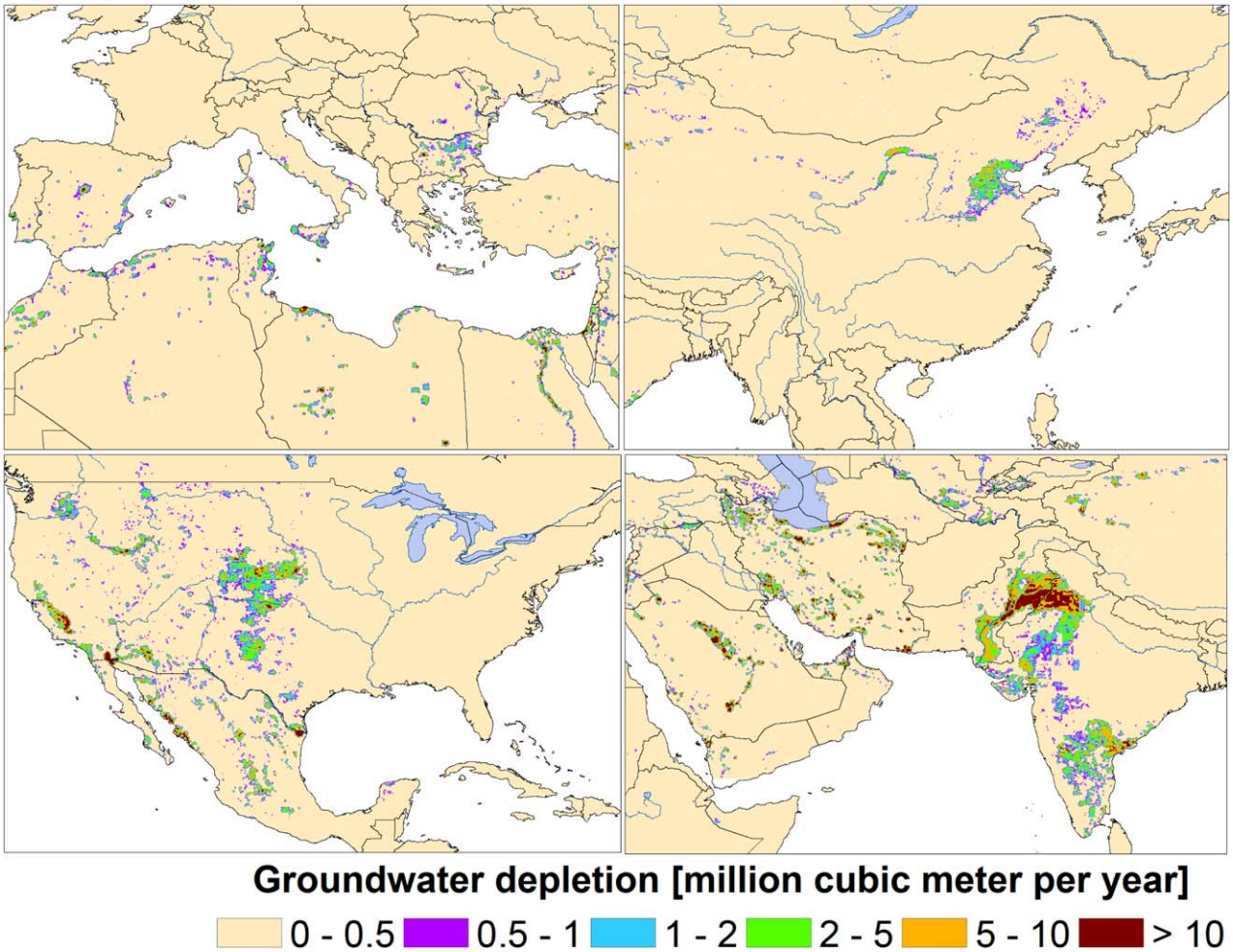

Figure 16. Groundwater depletion for the year 2010 at a 6 min spatial resolution. Global total equals 120 $km^3\ yr^{-1}$.

light-blue values give the result when all observations are included, in dark-blue are the result if only observations in sediment basins are included. The statistics for both runs (Figure 19) show that the model performance is best for sediment basins. The pristine run is slightly better than the human run. This is mainly due to regional scale groundwater heads in aquifers at higher elevations that decline and increase the bias between observed and simulated heads.

The global map of simulated groundwater heads shows regions with shallow groundwater depths including the major river basins and wetlands of the world. For these regions it is important to include lateral flows and define aquifers, as although groundwater flows are often slow they can be significant and often cross catchment or aquifer boundaries. The simulated groundwater heads show good agreement with observed data ($R^2 = 0.9$, $a = 0.76$). The groundwater discharge-recharge ratio shows the decline in groundwater base flow due to abstractions, highest for highly abstracted aquifers like the High Plains. Also, water budgets that are supported by inter-basin groundwater flows are no longer supported when abstractions are included. These results emphasize the need of including lateral flows and groundwater-surface water interactions in the current hydrological modeling efforts. Obviously the groundwater model used in this paper still has limitations and must be considered as a first-order attempt toward global groundwater modeling. Also, the inclusion of abstractions is in its pioneering status. The greatest limitation is that the current groundwater model runs at steady-state and only an upper unconfined aquifer is parameterized. It does not say anything about temporal changes in groundwater heads and information on vertical structure of the aquifers should be included as this holds vital information on the accessibility and quality of the global groundwater resource. Therefore, the results of the groundwater model have not yet been used to estimate groundwater

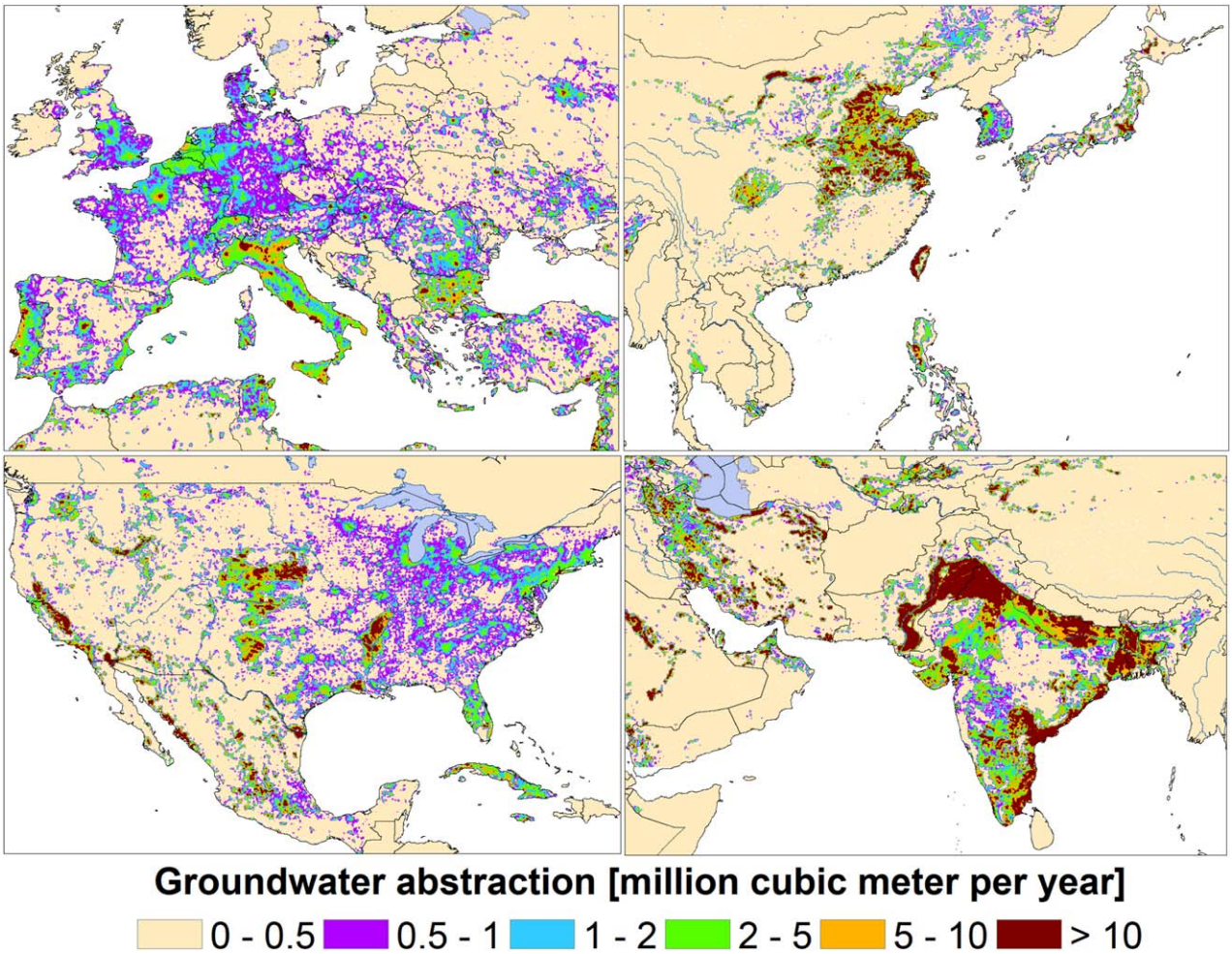

Figure 17. Groundwater abstraction for the year 2010 at a 6 min spatial resolution. Global total equals 1000 $km^3\ yr^{-1}$.

depletion. Vertical aquifer structure, head fluctuations and estimating groundwater depletion will be addressed in future work. It is expected that inclusion of lateral flows in depletion simulations would improve depletion estimates and fit reported groundwater heads better.

4.4. Comparison of Estimated Water Use to Reported Statistics

Our methodology to reconstruct past water use follows the approach of *Wada et al.* [2011a, 2011b, 2014]. In earlier work [*Wada et al.*, 2011a, 2011b, 2014], the methods and outputs used in this study have been extensively validated using available country water use statistics (FAO AQUASTAT) and estimates [*Shiklomanov*, 2000a, 2000b] for about 200 countries. Here we compare per country the estimated agricultural water withdrawal with the reported value taken from the FAO AQUASTAT database. Good agreements have been obtained from 1970 to 2000 for most countries including major agricultural water users such as India, China, United States, Pakistan and Mexico. But deviations are relatively large for Iraq, Finland, Austria, Central African Republic and Trinidad and Tobago. The reported values of the FAO AQUASTAT database are not available before 1970. Overall, R^2 and α range from 0.95 to 0.99 and from 0.88 to 1.10 respectively. Errors in prescribed irrigated areas, irrigation efficiency, and imprecise calendars of multiple cropping systems may have large influences on the discrepancy of the results. Irrigated areas and irrigation efficiency tend to be the two largest sources of the uncertainty simulating irrigation water use [*Döll and Siebert*, 2002; *Wisser et al.*, 2008]. Nevertheless, the deviations of estimated results are rather small for most countries and our model is generally capable of simulating regional variability of irrigation water use across the globe. Comparisons of estimated industrial water withdrawal per country with the reported values also show good correlations. R^2 is over 0.98 except for 1995 and α ranges from 0.82 to 0.99. Deviations are large for Argentina,

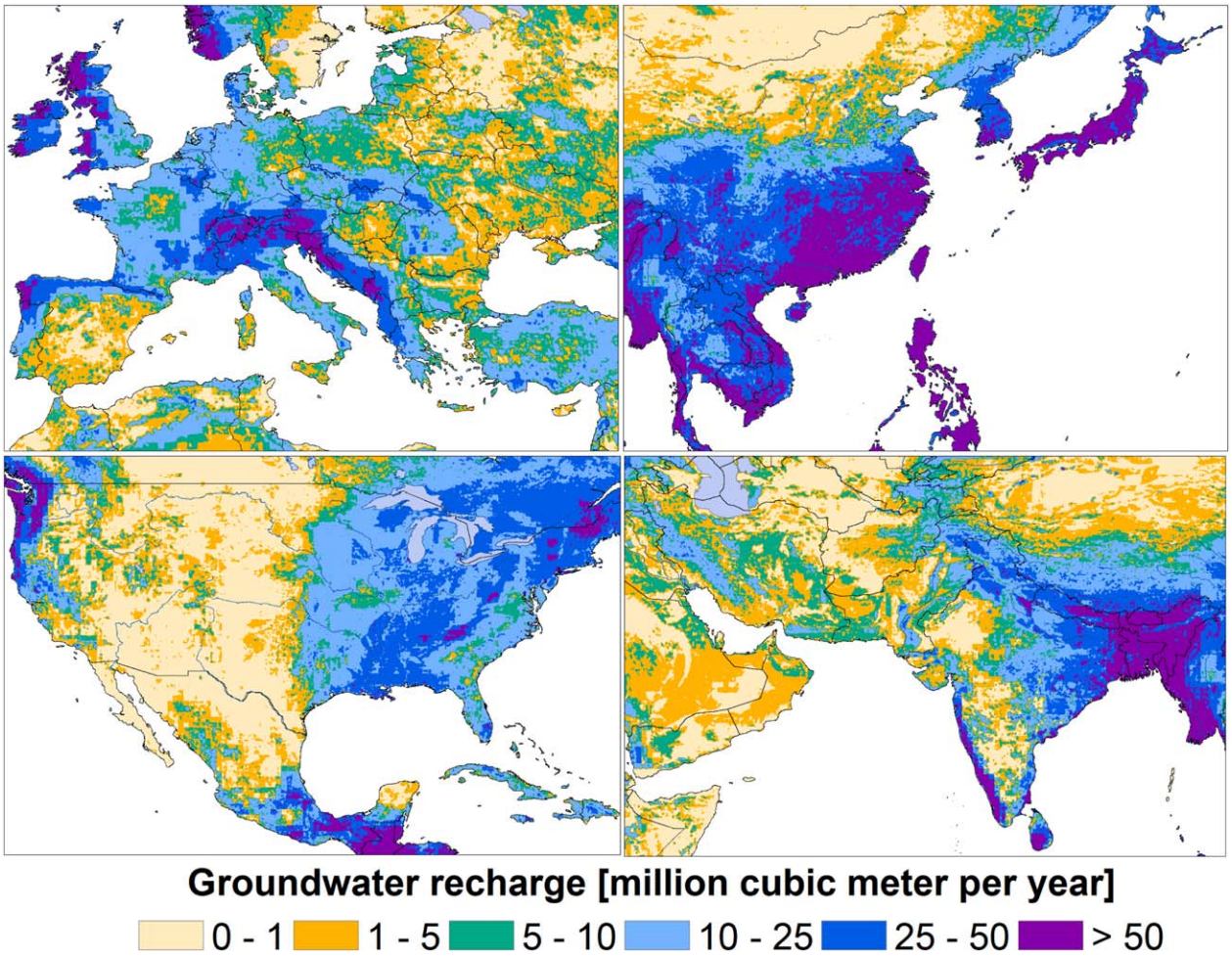

Figure 18. Long-term groundwater recharge including irrigation return flow over the period 1960–2010 at a 6min spatial resolution. Global total equals 18,000 km^3 yr^{-1}.

Ethiopia, Greece, Indonesia, Lebanon, Nicaragua, Panama, Puerto Rico and Turkmenistan where we generally overestimate the demand. Nevertheless, overall we have good agreements for most countries including major industrial water users such as United States, China, Germany, Canada and India. Comparison with the reported value per country also shows good agreement from 1970 to 2000 with R^2 being over 0.96. α ranges from 0.92 to 1.14. Although the correlations are high for most countries, deviations are relatively large for several countries, e.g., Iraq, Lithuania, Puerto Rico, Mali, Djibouti and Bhutan. Comparison of estimated gross total water demand with reported total water withdrawal per country shows good agreement, with R^2

Table 3. Comparison of Observed and Simulated Streamflow Under the Natural Conditions (N) and Under Human-Induced Change (Water Use and Reservoir Regulation) (H) for All Available GRDC Stations[a]

	Long-Term Statistics (N=2352)				Simulation Period 1960–2010 (N=2023)			
	α		R^2		α		R^2	
Monthly Discharge Q (m^3 s^{-1})	N	H	N	H	N	H	N	H
Average	0.90	0.92	0.92	0.95	0.92	0.96	0.93	0.96
Minimum	0.82	0.91	0.91	0.96	0.85	0.92	0.90	0.97
Maximum	0.89	0.91	0.82	0.85	0.94	0.95	0.82	0.88

[a]Evaluated are all long-term statistics from the GRDC inventory and those for stations with matching data (>10 years) over the simulation period 1960–2010. α (slope; x coordinate: simulated streamflow; y coordinate: observed streamflow) and R^2 (the coefficient of determination) have been calculated from comparison between monthly observed and simulated streamflow with the intercept forced through the origin.

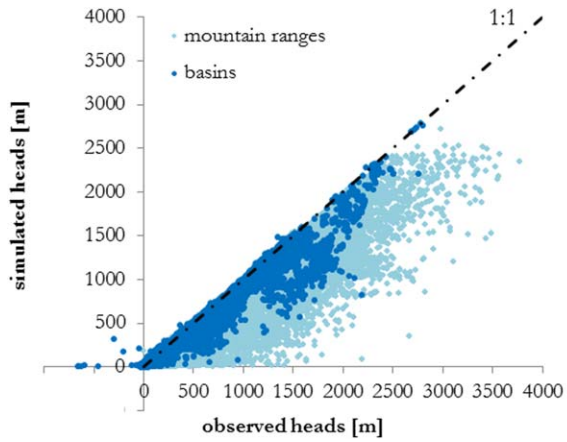

	Pristine	Human
R^2	0.9	0.9
α	0.76	0.75
R^2	0.96	0.95
α	0.86	0.83

Figure 19. Scatter plot of observed heads against simulated heads for the pristine run; in dark blue sediments basins, in light blue mountain ranges. Table presents statistics of both runs. Observed heads are based on a compilation of reported piezometer data [*Fan et al.*, 2013].

ranging from 0.97 to 0.99. The deviations observed in the sectoral comparisons become less apparent when summed over all of the sectoral demands. For Greece and Iraq (+50%), and Mali and Turkmenistan (−40%), the deviations remain large. Additional comparisons of estimated total water withdrawal and water consumption to those from *Shiklomanov* [2000a, 2000b] also show good agreements for most of the countries, with R^2 ranging from 0.94 to 0.98 and α ranging from 0.95 to 1.12.

5. Discussion and Conclusions

5.1. Limitations and Opportunities in Modeling Framework

Our high-resolution modeling framework has several major limitations. The model does not include any artificial water diversions such as aqueducts and inter-basin water transfer. Increasing water supply through water diversions tends to be a common response in water scarce regions with intense water use. Such diversions can supply additional water availability in some regions where extensive diversion works are present (e.g., India, United States, and China). In this study, human water consumption is subtracted from simulated streamflow that is routed through natural drainage networks only. This means that in some regions where extensive diversion works are present (the U.S., India and China) the reduction of streamflow due to water consumption is likely overestimated. Moreover, the results largely rely on the accuracy of estimated water use. The methods we used to estimate sectoral consumptive water in this study were tested, and the corresponding results were validated against available statistics and estimates in an earlier study [*Wada et al.*, 2014]. However, validation of simulated consumptive water use (per sector) remains difficult due to a lack of reliable information in many regions of the world.

Our high-resolution modeling framework enables more precise depiction of regional variability in water availability and use globally. This gives an opportunity to connect global assessments to regional and local scale issues. In this study, regional water scarcity was assessed at three different spatial scales. The grid scale approach underestimates water availability due to disconnection of water supply network, particularly in large urban areas (e.g, Paris, New York, Los Angeles, and Moscow), resulting in an overestimation of water scarcity. Subbasin- and county-scale approaches provide more accurate information of water availability per region, however, aggregation of grid cells ignores local variability in water use and stress. In addition, a county may not be a suitable unit for a water supply systems for some regions due to an extensive area. Further information on local water supply system needs to be integrated into high-resolution modeling framework in order to obtain more accurate estimate of water availability per region. Such information can be linked with river discharge and reservoir data in order to depict the overall human regulation in water supply system.

The improvement of high-performance computing enables running of a global simulation at a finer spatial scale than before. However, the model simulation can be constrained by data availability at fine spatial scales. For hydrologic simulation, several key inputs include climate forcings, soil properties, land use,

vegetation, elevation, and drainage network. Our modeling framework includes the vegetation, land surface parameters, and soil property data given originally at a ~0.01° spatial resolution. The drainage network and elevation data are also given at a ~0.01° spatial resolution or finer. However, the climate forcings remain at the coarse resolution of ~0.5°. In our model simulation, climate forcings have been downscaled to a 0.1° spatial resolution in order to represent finer vertical elevation transitions using lapse rates. This would, however, still yield large uncertainty in particular for precipitation of large spatial variability. This downscaling method is not able to resolve well local precipitation extremes. Finer climate forcings would substantially improve hydrologic model simulation at fine spatial scale (<0.1°).

To assess overexploitation of surface freshwater and groundwater resources, a state-of-the-art high-resolution global modeling framework has been developed. Our analysis of water availability, use and scarcity was carried out at policy relevant scales, that is at spatial and temporal scales that can indicate which parts of a region might be most vulnerable to change or in need of institutional attention. Our assessment builds upon previous modeling efforts and contributes to improve current knowledge that quantifies and distinguishes the impacts of human activities and climate variability on surface water and groundwater resources at the global scale. Despite the limitations, this modeling framework advances an important step beyond earlier work by attempting to account more accurately for regional variability in water availability and use. Demographic, socio-economic, technological, and land use change were reflected in growing human water use over time. Substantial regional variations were observed for the human and climate impacts on surface freshwater and groundwater resources, with humans having by far the largest impact on the terrestrial water system in various regions (e.g., India, Pakistan, China, United States, and the Middle East). In future work, this modeling framework can be further refined to approach more realistically various regional water issues (e.g., drought, flood, and sustainable water management), combining regional and local water data into a high-resolution global modeling framework.

Acknowledgments
We cordially thank two anonymous referees for their thorough review and constructive comments, which have substantially improved the quality of the manuscript. Y. Wada is supported by Japan Society for the Promotion of Science (JSPS) Oversea Research Fellowship (grant JSPS-2014-878). The PCR-GLOBWB model is an open source hydrological model that can be obtained from Utrecht University (http://www.globalhydrology.nl/models/pcr-globwb-2-0/).

References

Alcamo, J., M. Flörke, and M. Märker (2007), Future long-term changes in global water resources driven by socio-economic and climatic changes, *Hydrol. Sci. J.*, *52*, 247–275, doi:10.1623/hysj.52.2.247.

Allen, R. G., L. S. Pereira, D. Raes, and M. Smith (1998), Crop evapotranspiration—Guidelines for computing crop water requirements, *FAO Irrig. Drain. Pap. 56*, Food and Agric. Organ. of the U. N., Rome.

Arnell, N. W. (1999), Climate change and global water resources, *Global Environ. Change*, *9*, 31–49, doi:10.1016/S0959-3780(99)00017-5.

Arnell, N. W. (2004), Climate change and global water resources: SRES emissions and socio-economic scenarios, *Global Environ. Change*, *14*, 31–52, doi:10.1016/j.gloenvcha.2003.10.006.

Batjes, N. H. (2005), ISRIC-WISE—Global data set of derived soil properties on a 0.5 by 0.5 degree grid (Version 3.0), *Rep. 2005/08*, ISRIC—World Soil Inf., Wageningen, Netherlands. [Available at http://www.isric.org/data/isric-wise-global-data-set-derived-soil-properties-05-05-degree-grid-ver-30.]

Bierkens, M. F. P., et al. (2015), Hyper-resolution global hydrological modelling: What is next?, *Hydrol. Processes*, *29*, 310–320, doi:10.1002/hyp.10391.

Bondeau, A., P. C. Smith, S. Zaehle, S. Schaphoff, W. Lucht, W. Cramer, D. Gerten, M. Reichstein, and B. Smith (2007), Modelling the role of agriculture for the 20th century, *Global Change Biol.*, *13*, 679–706, doi:10.1111/j.1365-2486.2006.01305.x.

Dai, A. (2011), Drought under global warming: A review, *WIREs Clim. Change*, *2*, 45–65, doi:10.1002/wcc.81.

Dai, A. (2013), Increasing drought under global warming: Reconciling observed and model-simulated changes, *Nat. Clim. Change*, *3*, 52–58, doi:10.1038/nclimate1633.

Dankers, R., et al. (2014), First look at changes in flood hazard in the Inter-Sectoral Impact Model Intercomparison Project ensemble, *Proc. Natl. Acad. Sci. U. S. A.*, *111*(9), 3257–3261, doi:10.1073/pnas.1302078110.

Dee, D. P., et al. (2011), The ERA-Interim reanalysis: Configuration and performance of the data assimilation system, *Q. J. R. Meteorol. Soc.*, *137*, 553–597, doi:10.1002/qj.828.

de Graaf, I. E. M., L. P. H. van Beek, Y. Wada, and M. F. P. Bierkens (2014), Dynamic attribution of global water demand to surface water and groundwater resources: Effects of abstractions and return flows on river discharges, *Adv. Water Resour.*, *64*, 21–33, doi:10.1016/j.advwatres.2013.12.002.

de Graaf, I. E. M., E. H. Sutanudjaja, L. P. H. van Beek, and M. F. P. Bierkens (2015), A high-resolution global-scale groundwater model, *Hydrol. Earth Syst. Sci.*, *19*, 823–837, doi:10.5194/hess-19-823-2015.

Döll, P., and S. Siebert (2002), Global modeling of irrigation water requirements, *Water Resour. Res.*, *38*(4), 1037, doi:10.1029/2001WR000355.

Döll, P., F. Kaspar, and B. Lehner (2003), A global hydrological model for deriving water availability indicators: Model tuning and validation, *J. Hydrol.*, *270*, 105–134, doi:10.1016/S0022-1694(02)00283-4.

Döll, P., H. Hoffmann-Dobrev, F. T. Portmann, S. Siebert, A. Eicker, M. Rodell, and G. Strassberg (2012), Impact of water withdrawals from groundwater and surface water on continental water storage variations, *J. Geodyn.*, 59–60, doi:10.1016/j.jog.2011.05.001.

Ek, M. B., K. E. Mitchell, Y. Lin, E. Rogers, P. Grunmann, V. Koren, G. Gayno, and J. D. Tarpley (2003), Implementation of Noah land surface model advances in the National Centers for Environmental Prediction operational mesoscale Eta model, *J. Geophys. Res.*, *108*(D22), 8851, doi:10.1029/2002JD003296.

Elliott, J., et al. (2014), Constraints and potentials of future irrigation water availability on agricultural production under climate change, *Proc. Natl. Acad. Sci. U. S. A.*, *111*(9), 3239–3244, doi:10.1073/pnas.1222474110.

Falkenmark, M., J. W. Kijne, B. Taron, G. Murdoch, M. V. K. Sivakumar, and E. Craswell (1997), Meeting water requirements of an expanding world population [and discussion], *Philos. Trans. R. Soc. London B*, *352*, 929–936, doi:10.1098/rstb.1997.0072.

Famiglietti, J. S., M. Lo, S. L. Ho, J. Bethune, K. J. Anderson, T. H. Syed, S. C. Swenson, C. R. de Linage, and M. Rodell (2011), Satellites measure recent rates of groundwater depletion in California's Central Valley, *Geophys. Res. Lett.*, *38*, L03403, doi:10.1029/2010GL046442.

Fan, Y., H. Li, and G. Miguez-Macho (2013), Global patterns of groundwater table depth, *Science*, *339*, 940–943, doi:10.1126/science.1229881.

Feyen, L., and R. Dankers (2009), Impact of global warming on streamflow drought in Europe, *J. Geophys. Res.*, *114*, D17116, doi:10.1029/2008JD011438.

Food and Agriculture Organization of the United Nations (FAO) (2003), *Digital Soil Map of the World, Version 3.6*, Rome. [Available at http://www.fao.org/nr/land/soils/digital-soil-map-of-the-world.]

Food and Agriculture Organization of the United Nations (FAO) (2007), *Gridded Livestock of the World 2007*, edited by G. R. W. Wint and T. P. Robinson, 131 pp., Rome. Available online at http://www.fao.org/docrep/010/a1259e/a1259e00.HTM

Freydank, K., and S. Siebert (2008), Towards mapping the extent of irrigation in the last century: Time series of irrigated area per country, *Frankfurt Hydrol. Pap. 08*, Inst. of Phys. Geogr., Univ. of Frankfurt, Frankfurt am Main, Germany.

Gain, A. K., and Y. Wada (2014), Assessment of future water scarcity at different spatial and temporal scales of the Brahmaputra River Basin, Water *Resour. Manage.*, *28*, 999–1012, doi:10.1007/s11269-014-0530-5.

Gerten, D., S. Schaphoff, and W. Lucht (2007), Potential future changes in water limitation of the terrestrial biosphere, *Clim. Change*, *80*, 277–299, doi:10.1007/s10584-006-9104-8.

Gleeson, T., and Y. Wada (2013), Assessing regional groundwater stress for nations using multiple data sources with the groundwater footprint, *Environ. Res. Lett.*, *8*, 044010, doi:10.1088/1748-9326/8/4/044010.

Gleeson, T., L. Smith, N. Moosdorf, J. Hartmann, H. H. Dürr, A. H. Manning, L. P. H. van Beek, and A. M. Jellinek (2011), Mapping permeability over the surface of the Earth, *Geophys. Res. Lett.*, *38*, L02401, doi:10.1029/2010GL045565.

Gleeson, T., Y. Wada, M. F. P. Bierkens, and L. P. H. van Beek (2012), Water balance of global aquifers revealed by groundwater footprint, *Nature*, *488*, 197–200, doi:10.1038/nature11295.

Gleeson, T., N. Moosdorf, J. Hartmann, and L. P. H. van Beek (2014), A glimpse beneath earth's surface: GLobal HYdrogeology MaPS (GLHYMPS) of permeability and porosity, *Geophys. Res. Lett.*, *41*, 3891–3898, doi:10.1002/2014GL059856.

Gleick, P. H. (2003), Global freshwater resources: Soft-path solutions for the 21st century, *Science*, *302*, 1524–1528, doi:10.1126/science.1089967.

Gleick, P. H. (2010), Roadmap for sustainable water resources in southwestern North America, Proc. *Natl. Acad. Sci. U. S. A.*, *107*, 21,300–21,305, doi:10.1073/pnas.1005473107.

Haddeland, I., et al. (2014), Global water resources affected by human interventions and climate change, *Proc. Natl. Acad. Sci. U. S. A.*, *111*(9), 3251–3256, doi:10.1073/pnas.1302078110.

Hagemann, S. (2002), *An Improved Land Surface Parameter Dataset for Global and Regional Climate Models*, Max-Planck-Inst. für Meteorol., Hamburg, Germany.

Hagemann, S., and L. D. Gates (2003), Improving a sub-grid runoff parameterization scheme for climate models by the use of high resolution data derived from satellite observations, *Clim. Dyn.*, *21*, 349–359, doi:10.1007/s00382-003-0349-x.

Hanasaki, N., S. Kanae, and T. Oki (2006), A reservoir operation scheme for global river routing models, *J. Hydrol.*, *327*, 22–41, doi:10.1016/j.jhydrol.2005.11.011.

Hanasaki, N., S. Kanae, T. Oki, K. Masuda, K. Motoya, N. Shirakawa, Y. Shen, and K. Tanaka (2008a), An integrated model for the assessment of global water resources—Part 1: Model description and input meteorological forcing, *Hydrol. Earth Syst. Sci.*, *12*, 1007–1025, doi:10.5194/hess-12-1007-2008.

Hanasaki, N., S. Kanae, T. Oki, K. Masuda, K. Motoya, N. Shirakawa, Y. Shen, and K. Tanaka (2008b), An integrated model for the assessment of global water resources—Part 2: Applications and assessments, *Hydrol. Earth Syst. Sci.*, *12*, 1027–1037, doi:10.5194/hess-12-1027-2008.

Harbaugh, A. W., E. R. Banta, M. C. Hill, and M. G. McDonald (2000), MODFLOW-2000, The U.S. Geological Survey Modular Ground-Water Model - User guide to modularization concepts and the ground-water flow process, U.S. Geological Survey Open-File Report 00-92, 121 pp., Reston, Va. [Available online at http://pubs.usgs.gov/of/2000/0092/report.pdf.]

Hartmann, J., and N. Moosdorf (2012), The new global lithological map database GLiM: A representation of rock properties at the Earth surface, *Geochem. Geophys. Geosyst.*, *13*, Q12004, doi:10.1029/2012GC004370.

Hoekstra, A. Y., M. M. Mekonnen, A. K. Chapagain, R. E. Mathews, and B. D. Richter (2012), Global monthly water scarcity: Blue water footprints versus blue water availability, *PLoS One*, *7*, e32688, doi:10.1371/journal.pone.0032688.

Jung, M., et al. (2010), Recent decline in the global land evapotranspiration trend due to limited moisture supply, *Nature*, *467*, 951–954, doi:10.1038/nature09396.

Klein Goldewijk, K. and G. van Drecht (2006), HYDE 3: Current and historical population and land cover, MNP, edited by A. F. Bouwman, T. Kram and K. K. Goldewijk, Integrated modelling of global environmental change, An overview of IMAGE 2.4, Netherlands Environmental Assessment Agency (MNP), Bilthoven, Netherlands.

Konikow, L. F. (2011), Contribution of global groundwater depletion since 1900 to sea-level rise, *Geophys. Res. Lett.*, *38*, L17401, doi:10.1029/2011GL048604.

Konikow, L. F., and E. Kendy (2005), Groundwater depletion: A global problem, *Hydrogeol. J.*, *13*, 317–320, doi:10.1007/s10040-004-0411-8.

Kraijenhoff van de Leur, D. A. (1958), A study of non-steady ground-water flow with special reference to the reservoir-coefficient, *De Ingenieur*, *19*, 87–94.

Kummu, M., P. J. Ward, H. de Moel, and O. Varis (2010), Is physical water scarcity a new phenomenon? Global assessment of water shortage over the last two millennia, *Environ. Res. Lett.*, *5*, 034006, doi:10.1088/1748-9326/5/3/034006.

Landerer F. W., and S. C. Swenson (2012), Accuracy of scaled GRACE terrestrial water storage estimates. *Water Resour. Res.*, *48*, W04531, doi:10.1029/2011WR011453.

Lehner, B., et al. (2011), High-resolution mapping of the world's reservoirs and dams for sustainable river-flow management, *Frontiers Ecol. Environ.*, *9*, 494–502, doi:10.1890/100125.

Liu, J., and H. Yang (2010), Spatially explicit assessment of global consumptive water uses in cropland: Green and blue water, *J. Hydrol.*, *384*, 187–297, doi:10.1016/j.jhydrol.2009.11.024.

Mitchell, T. D., and P. D. Jones (2005), An improved method of constructing a database of monthly climate observations and associated high-resolution grids, *Int. J. Clim.*, *25*, 693–712, doi:10.1002/joc.1181.

Nash, J. E., and J. V. Sutcliffe (1970), River flow forecasting through conceptual models part I – A discussion of principles, *J. Hydrol.*, *10*, 282–290.

Oki, T., and S. Kanae (2006), Global hydrological cycles and world water resources, *Science*, *313*, 1068–1072, doi:10.1126/science.1128845.

Pokhrel, Y., N. Hanasaki, S. Koirala, J. Cho, P. J.-F. Yeh, H. Kim, S. Kanae, and T. Oki (2012), Incorporating anthropogenic water regulation modules into a land surface model, *J. Hydrometeorol.*, *13*, 255–269, doi:10.1175/JHM-D-11-013.1.

Portmann, F. T., S. Siebert, and P. Döll (2010), MIRCA2000—Global monthly irrigated and rainfed crop areas around the year 2000: A new high-resolution data set for agricultural and hydrological modeling, *Global Biogeochem. Cycles*, *24*, GB1011, doi:10.1029/2008GB003435.

Prudhomme, C., et al. (2014), Drought in the 21st century: A multi-model ensemble experiment to assess global change, quantify uncertainty and identify 'hotspots', change, *Proc. Natl. Acad. Sci. U. S. A.*, *111*(9), 3262–3267, doi:10.1073/pnas.1222473110.

Rodell, M., I. Velicogna, and J. S. Famiglietti (2009), Satellite-based estimates of groundwater depletion in India, *Nature*, *460*, 999–1002, doi:10.1038/nature08238.

Rost, S., D. Gerten, A. Bondeau, W. Luncht, J. Rohwer, and S. Schaphoff (2008), Agricultural green and blue water consumption and its influence on the global water system, *Water Resour. Res.*, *44*, W09405, doi:10.1029/2007WR006331.

Scanlon, B. R., I. Jolly, M. Sophocleous, and L. Zhang (2007), Global impacts of conversions from natural to agricultural ecosystems on water resources: Quantity versus quality, *Water Resour. Res.*, *43*, W03437, doi:10.1029/2006WR005486.

Scanlon, B. R., C. C. Faunt, L. Longuevergne, R. C. Reedy, W. M. Alley, V. L. McGuire, and P. B. McMahon (2012a), Groundwater depletion and sustainability of irrigation in the U.S. High Plains and Central Valley, *Proc. Natl. Acad. Sci. U. S. A.*, *109*, 9320–9325, doi:10.1073/pnas.1200311109.

Scanlon, B. R., L. Longuevergne, and D. Long (2012b), Ground referencing GRACE satellite estimates of groundwater storage changes in the California Central Valley, USA, *Water Resour. Res.*, *48*, W04520, doi:10.1029/2011WR011312.

Schaller, M. F., and Y. Fan (2009), River basins as groundwater exporters and importers: Implications for water cycle and climate modeling, *J. Geophys. Res.*, *114*, D04103, doi:10.1029/2008JD010636.

Schewe, J., et al. (2014), Multi-model assessment of water scarcity under climate change, *Proc. Natl. Acad. Sci. U. S. A.*, *111*(9), 3245–3250, doi:10.1073/pnas.1222460110.

Seager, R. (2007), The turn of the century North American Drought: Global context, dynamics, and past analogs, *J. Clim.*, *20*, 5527–5552, doi:10.1175/2007JCLI1529.1.

Sheffield, J., and E. F. Wood (2007), Characteristics of global and regional drought, 1950–2000: Analysis of soil moisture data from off-line simulation of the terrestrial hydrologic cycle, *J. Geophys. Res.*, *112*, D17115, doi:10.1029/2006JD008288.

Sheffield, J., E. F. Wood, and M. L. Roderick (2012), Little change in global drought over the past 60 years, *Nature*, *491*, 435–438, doi:10.1038/nature11575.

Shiklomanov, I. A. (1997), *Assessment of Water Resources and Water Availability in the World, Comprehensive Assessment of the Freshwater Resources of the World*, World Meteorol. Organ. and the Stockholm Environ. Inst., Stockholm.

Shiklomanov, I. A. (2000a), World water resources and water use: Present assessment and outlook for 2025, in *World Water Scenarios Analyses*, edited by F. R. Rijsberman, pp. 160–203, Earthscan, London, U. K.

Shiklomanov, I. A. (2000b), Appraisal and assessment of world water resources, *Water Int.*, *25*, 11–32, doi:10.1080/02508060008686794.

Siebert, S., and P. Döll (2010), Quantifying blue and green virtual water contents in global crop production as well as potential production losses without irrigation, *J. Hydrol.*, *384*, 198–217, doi:10.1016/j.jhydrol.2009.07.031.

Siebert, S., J. Burke, J. M. Faures, K. Frenken, J. Hoogeveen, P. Döll, and F. T. Portmann (2010), Groundwater use for irrigation – a global inventory, *Hydrol. Earth Syst. Sci.*, *14*, 1863–1880, doi:10.5194/hess-14-1863-2010.

Steinfeld, H., P. Gerber, T. Wassenaar, V. Castel, M. Rosales, and C. de Haan (2006), *Livestocks Long Shadow: Environmental Issues and Options*, FAO, Rome, ISBN 978-92-5-105571-7.

Sutanudjaja, E. H., L. P. H. van Beek, S. M. de Jong, F. C. van Geer, and M. F. P. Bierkens (2014), Calibrating a large-extent high-resolution coupled groundwater-land surface model using soil moisture and discharge data, *Water Resour. Res.*, *50*, 687–705, doi:10.1002/2013WR013807.

Tang, Q., T. Oki, S. Kanae, and H. Hu (2007), The inuence of precipitation variability and partial irrigation within grid cells on a hydrological simulation, *J. Hydrometeorol.*, *8*, 499–512, doi:10.1175/JHM589.1.

Taylor, R. G., et al. (2013), Groundwater and climate change, *Nat. Clim. Change*, *3*, 322–329, doi:10.1038/nclimate1744.

Tiwari, V.M., J. Wahr, and S. Swenson (2009), Dwindling groundwater resources in northern India, from satellite gravity observations, *Geophys. Res. Lett.*, *36*, L18401, doi:10.1029/2009GL039401.

Todini, E. (1996), The ARNO rainfall–runoff model, *J. Hydrol.*, *175*, 339–382, doi:10.1016/S0022-1694(96)80016-3.

Trenberth, K. E., G. W. Branstator, and P. A. Arkin (1988), Origins of the 1988 North American Drought, *Science*, *242*, 1640–1645, doi:10.1126/science.242.4886.1640.

Uppala, S. M., et al. (2005), The ERA-40 re-analysis, *Q. J. R. Meteorol. Soc.*, *131*, 2961–3012, doi:10.1256/qj.04.176.

Van Beek, L. P. H., Y. Wada, and M. F. P. Bierkens (2011), Global monthly water stress: 1. Water balance and water availability, *Water Resour. Res.*, *47*, W07517, doi:10.1029/2010WR009791.

Van Dijk, A. I. J. M., L. J. Renzullo, Y. Wada, and P. Tregoning (2014), A global water cycle reanalysis (2003–2012) merging satellite gravimetry and altimetry observations with a hydrological multi-model ensemble, *Hydrol. Earth Syst. Sci.*, *18*, 2955–2973, doi:10.5194/hess-18-2955-2014.

Vörösmarty, C. J., B. M. Fekete, M. Meybeck, and R. B. Lammers (2000), Global system of rivers: Its role in organizing continental land mass and defining land-to-ocean linkages, *Global Biogeochem. Cycles*, *14*(2), 599–621, doi:10.1029/1999GB900092.

Vörösmarty, C. J., C. Leveque, and C. Revenga (2005), Freshwater ecosystems, in Millennium Ecosystem Assessment, vol. 1, Conditions and Trends, edited by C. Caudill et al., chap. 7, pp. 165–207, Island Press, Washington, D. C.

Vörösmarty, C. J., P. McIntyre, M. O. Gessner, D. Dudgeon, A. Prusevich, P. Green, S. Glidden, S. E. Bunn, C. A. Sullivan, and C. R. Liermann (2010), Global threats to human water security and river biodiversity, *Nature*, *467*, 555–561, doi:10.1038/nature09440.

Wada, Y., and L. Heinrich (2013), Assessment of transboundary aquifers of the world—vulnerability arising from human water use, *Environ. Res. Lett.*, *8*, 024003, doi:10.1088/1748-9326/8/2/024003.

Wada, Y., L. P. H. van Beek, and M. F. P. Bierkens (2011a), Modelling global water stress of the recent past: on the relative importance of trends in water demand and climate variability, *Hydrol. Earth Syst. Sci.*, *15*, 3785–3808, doi:10.5194/hess-15-3785-2011.

Wada, Y., L. P. H. van Beek, D. Viviroli, H. H. Dürr, R. Weingartner, and M. F. P. Bierkens (2011b), Global monthly water stress: 2. Water demand and severity of water stress, *Water Resour. Res.*, *47*, W07518, doi:10.1029/2010WR009792.

Wada, Y., L. P. H. van Beek, and M. F. P. Bierkens (2012a), Nonsustainable groundwater sustaining irrigation: A global assessment, *Water Resour. Res.*, *48*, W00L06, doi:10.1029/2011WR010562.

Wada, Y., L. P. H. van Beek, F. C. Sperna Weiland, B. F. Chao, Y.-H. Wu, and M. F. P. Bierkens (2012b), Past and future contribution of global groundwater depletion to sea-level rise, *Geophys. Res. Lett.*, *39*, L09402, doi:10.1029/2012GL051230.

Wada, Y., L. P. H. van Beek, N. Wanders, and M. F. P. Bierkens (2013), Human water consumption intensifies hydrological drought worldwide, *Environ. Res. Lett.*, *8*, 034036, doi:10.1088/1748-9326/8/3/034036.

Wada, Y., D. Wisser, and M. F. P. Bierkens (2014), Global modeling of withdrawal, allocation and consumptive use of surface water and groundwater resources, *Earth Syst. Dyn.*, *5*, 15–40, doi:10.5194/esd-5-15-2014.

Widén-Nilsson, E., S. Halldin, and C.-Y. Xu (2007), Global water-balance modelling with WASMOD-M: Parameter estimation and regionalization, *J. Hydrol.*, *340*, 105–118, doi:10.1016/j.jhydrol.2007.04.002.

Wisser, D., S. Frolking, E. M. Douglas, B. M. Fekete, C. J. Vörösmarty, and A. H. Schumann (2008), Global irrigation water demand: Variability and uncertainties arising from agricultural and climate data sets, *Geophys. Res. Lett.*, *35*, L24408, doi:10.1029/2008GL035296.

Wisser, D., B. M. Fekete, C. J. Vörösmarty, and A. H. Schumann (2010), Reconstructing 20th century global hydrography: A contribution to the Global Terrestrial Network- Hydrology (GTN-H), *Hydrol. Earth Syst. Sci.*, *14*, 1–24, doi:10.5194/hess-14-1-2010.

Wood, E. F., D. P. Lettenmaier, and V. G. Zartarian (1992), A land-surface hydrology parameterization with subgrid variability for general circulation models, *J. Geophys. Res.*, *97*(D3), 2717–2728, doi:10.1029/91JD01786.

Wood, E. F., et al. (2011), Hyperresolution global land surface modeling: Meeting a grand challenge for monitoring Earth's terrestrial water, *Water Resour. Res.*, *47*, W05301, doi:10.1029/2010WR010090.

World Resources Institute (WRI) (1998), *World Resources: A Guide to the Global Environment 1998–99*, Washington, D. C.